

Guidelines to use input contact parameters for nonlinear dynamic analysis of jointed structures: Results of a round robin test

*Original*

Guidelines to use input contact parameters for nonlinear dynamic analysis of jointed structures: Results of a round robin test / Fantetti, Alfredo; Botto, Daniele; Zucca, Stefano; Schwingshackl, Christoph. - In: TRIBOLOGY INTERNATIONAL. - ISSN 0301-679X. - ELETTRONICO. - 191:(2024). [10.1016/j.triboint.2023.109158]

*Availability:*

This version is available at: 11583/2984520 since: 2023-12-15T06:41:20Z

*Publisher:*

Elsevier

*Published*

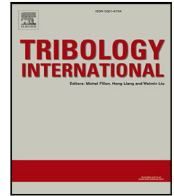
DOI:10.1016/j.triboint.2023.109158

*Terms of use:*

This article is made available under terms and conditions as specified in the corresponding bibliographic description in the repository

*Publisher copyright*

(Article begins on next page)



## Full Length Article

# Guidelines to use input contact parameters for nonlinear dynamic analysis of jointed structures: Results of a round robin test

Alfredo Fantetti <sup>a,\*</sup>, Daniele Botto <sup>b</sup>, Stefano Zucca <sup>b</sup>, Christoph Schwingshackl <sup>a</sup>

<sup>a</sup> Department of Mechanical Engineering, Imperial College London, Exhibition Rd, SW7 2BU, London, UK

<sup>b</sup> Department of Mechanical Engineering, Politecnico di Torino, Corso Duca degli Abruzzi, 10129, Torino, Italy

## ARTICLE INFO

## Keywords:

Jointed structures  
Friction hysteresis loops  
Tangential contact stiffness  
Friction coefficient  
Wear  
Nonlinear dynamic analysis

## ABSTRACT

Turbomachinery and other jointed structures are carefully designed to optimise their dynamic response and prevent unwanted high-cycle fatigue failures due to vibration. Advanced numerical models are employed to predict the often nonlinear dynamic responses, but their reliability is partially limited by the lack of understanding of the friction mechanisms between the vibrating contact interfaces. Although several high-frequency friction rigs have been developed at different institutions to measure contact parameters such as friction coefficient and contact stiffness, a lack of direct comparisons prevents a throughout understanding. To address this issue, a comparison of these contact parameters has been performed by employing the high-frequency friction rigs of Imperial College London and Politecnico di Torino. A test plan was designed to cover a wide experimental space by testing the friction rigs to their limits and measuring hysteresis loops under a range of normal loads and displacement amplitudes at room temperature. Measurements from the two very different experimental setups are compared, showing a good level of agreement for the friction coefficient, but also highlighting some differences, especially for the contact stiffness. New insights are provided into the physics of these contact parameters and specific guidelines are given to improve contact models used for nonlinear dynamic analysis.

## 1. Introduction

Many engineering structures employ friction joints to connect components, facilitating the assembly and guaranteeing structural integrity. Under vibration, the friction joints can impact the dynamic response of the jointed structure [1]. For example, they dissipate energy that results in a beneficial reduction of vibration amplitudes but can also induce wear [2–4], which is detrimental for the contacting components. Both these effects are strongly nonlinear with the excitation amplitude. Friction joints can also impact the resonant frequencies because of the additional contact stiffness associated with relative motion between the contacting components, which is also a nonlinear function of the excitation amplitude. These strong nonlinear effects on the dynamic response might result into unexpected stresses in the structure, which can eventually lead to high cycle fatigue failures of components [5]. It is therefore important to correctly model the behaviour of friction joints under vibration, with the aim of optimising their performance (more damping, better repeatability, more robustness [6]), understanding their wear behaviour and predicting correct resonance frequencies. Many of the current modelling approaches base their predictive capabilities on the discretisation of the contact interfaces [1,7] and on the

use of hysteresis loops to capture the underlying friction mechanisms across the interface [8], namely stick, slip and separation contact states. Such contact states drive nonlinear phenomena such as energy dissipation and contact stiffening that have a major impact on the dynamic response of the structure, e.g. by changing its damping and resonance frequencies. Contact parameters such as friction coefficient and contact stiffness are required to accurately represent these contact states, but their modelling is challenging due to a lack of high-quality validation data from the contact interfaces [4]. It is in fact challenging to experimentally capture what is happening locally at the interface during high-frequency vibration without interfering with the contact interface itself. This lack of validation data prevents the development of fully-validated and predictive modelling approaches and, as a result, expensive physical testing is required to assess the performance and reliability of new designs.

Several experimental techniques have been developed to measure the contact states and their characterising contact parameters. Some experimental techniques enable direct access to the contact interfaces, such as ultrasound measurements that are based on acoustic waves propagating through contacting components [9–14], or optical

\* Corresponding author.

E-mail address: [a.fantetti@imperial.ac.uk](mailto:a.fantetti@imperial.ac.uk) (A. Fantetti).

measurements based on laser illuminating transparent materials in contact [15–19]. These techniques provide however only partial information about the interface parameters. Ultrasonic measurements cannot determine whether changes in the contact states are induced by load variations in the normal or in the tangential/sliding directions [13], while optical measurements only provide information on contact interfaces of transparent materials, thus not being applicable to common metal-to-metal dry friction joints. Other techniques obtain information from metallic contacts indirectly, e.g. by measuring the global dynamic response of the jointed assembly [20–31], leading to a global representation of the joint in the structure, without a detailed knowledge of its physical behaviour. Most of these studies either calibrated the numerical dynamic responses to match the experimental ones or investigated the effects of variations of contact stiffness and friction coefficient on the global dynamic forced response. The shortcoming of those global measurements is that contact parameter estimations strongly depend on the particular dynamics of the investigated assembly and are thus not easily transferable to other load cases or other structures [28].

Given these limitations, the most common way to provide the input contact parameters for explicit nonlinear dynamic analysis is based on the traditional force–displacement measurements, i.e. hysteresis loops<sup>1</sup> [8]. Several research groups conducted a variety of experiments in the past decades to measure hysteresis loops [35–43] leading to a wide range of available input data for nonlinear models. Most of these studies performed measurements at low excitation frequencies or focused only on the friction coefficient and not on the contact stiffness, which is an important contact parameter for the nonlinear dynamic analysis of jointed structures. For nonlinear dynamic analysis, hysteresis loops are preferably measured at high frequencies similar to those experienced by the studied structures, by using purposely designed test rigs [44–54]. Those rigs provide also accurate displacement measurements with optical non-contact techniques based on either Laser Doppler vibrometer (LDV) measurements [44,45,47] or digital image correlation (DIC) with high-speed cameras [46,55–59]. Both LDV and DIC measurements have been used to monitor the motion of the boundaries of friction joint interfaces during a vibration cycle, making it possible to observe several contact phenomena, such as stick–slip transition at the edges of the contact, opening and closing of the contact and identification of permanent gaps. The main limitation of hysteresis measurements is however that measurement points are not located exactly on the interface but tens of micrometres far from it, on the side of the contacting components. Therefore, they only provide one- or two-dimensional information from the edge of the contact interface, without providing any insight into the behaviour of the central part of the contact. The information on the full contact behaviour is then still relying on numerical models to predict what is happening inside, with only a few validation data coming from experimental evidence at the edges. As a result, high reliability is required in hysteresis measurements to prevent major errors in simulations. The reliability of existing measurements is however partly limited by the individual capabilities of the high-frequency test rigs available at different institutions. These friction rigs do not often cover all measurement ranges of interest. In addition, a lack of direct comparisons between different rigs and a lack of a standardised approach for conducting measurements leads to low confidence in the measured parameters.

The objective of this work is to compare and discuss the reliability of contact parameters measured with different test rigs in different laboratories, to obtain a better understanding of their reliability and

<sup>1</sup> Note that, to measure the friction coefficient, many other methods exist [32], including pin on disc, weights hanging on a pulley, tilting of inclined planes, deflection of a pendulum or a spring and so on. Other friction analyses are related to earthquakes, which have long been recognised as being the result of stick–slip frictional instabilities [33,34].

new insights on the physics of contact mechanisms. To this end, a comprehensive round robin test is performed on two high-frequency friction rigs at Imperial College London [44] and Politecnico di Torino [45], hereafter referred to as Imperial and PoliTO, respectively. The round robin test consisted of recording comparable hysteresis loops on specimen pairs manufactured from the same batch of raw stainless steel. Tests were performed at room temperature under a wide range of test conditions, including different normal loads, displacement amplitudes, and nominal areas of contact providing a set of values of friction coefficient and tangential contact stiffness. Experimental results are open data, available in [60] for use by the scientific community. Insights into the physics are also given and recommendations are provided to improve contact models used for nonlinear dynamic analysis.

The paper is organised as follows. Section 2 briefly describes the physics of the hysteresis loops and the friction rigs used in the experimental campaign, underlying their differences and similarities. Section 3 details the test plan, the specimens geometries and the post-processing of the measured data. Section 4 shows the measured hysteresis loops and how wear affects their evolution. Section 5 compares the contact parameters obtained from the two friction rigs, discussing the role of the worn area of contact, the normal load and the displacement amplitude. A guideline for providing accurate input contact parameters for nonlinear dynamic analysis is reported in Section 6. The closure in Section 7 summarises the experimental findings and highlights the reliability of the measured contact parameters for nonlinear dynamic simulations.

## 2. Hysteresis loops and friction rigs used for the round robin test

The round robin focuses on the measurement of hysteresis loops, which are the cyclic load–deflection curves that plot the friction force against the relative displacement occurring between two oscillating contact interfaces. Fig. 1a shows a typical hysteresis loop, which is characterised by the following contact states:

- *Stick state* occurs right after the reversal of motion, ①→② or ④→⑤. In this contact state, the tangential contact force is linearly related to the relative displacement via the tangential contact stiffness  $k_t$ . The tangential contact stiffness can be obtained from the measured slope and is due to the elastic deformation of the micro-asperities at the contact interfaces [61] and the bulk elastic deformation at the macroscopic contact scale [62]. The tangential contact stiffness is an important parameter for the accurate prediction of the dynamic response of jointed structures, since it might strongly affect the resonant frequencies of the system [63].
- *Microslip* occurs during the transition between the stick regime and the gross slip regime, ②→③ or ⑤→⑥, and is due to a partial slip at the contact interfaces because a portion of the area of contact is still stuck (i.e. asperities elastically deform) while the remaining portion starts to slip. It appears with a progressive flattening of the tangential contact force before it transitions to gross slip.
- *Gross slip* occurs when the whole contact interface experiences a full relative sliding motion, ③→④ or ⑥→①. During gross slip, the friction force is approximately constant, although non-Coulomb friction conditions can sometimes occur [64–66], and is equal to the friction limit  $\mu N$ , where  $\mu$  and  $N$  are the friction coefficient and the normal load respectively. Mainly during gross slip the hysteresis loop dissipates energy, which is quantified by the area inside the loop itself. This dissipated energy is an important parameter for the nonlinear dynamic analysis, since it affects the damping, and hence the response amplitude of the system, but also drives the wear of the interfaces. The gross slip regime is also referred to as macroslip.

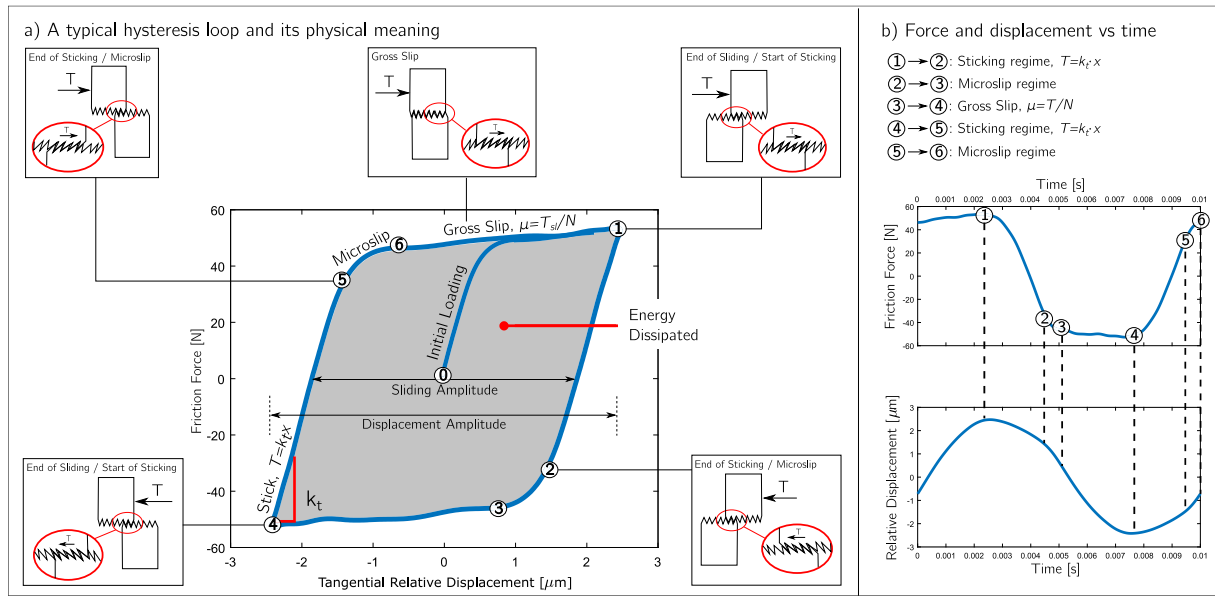


Fig. 1. A typical hysteresis loop: (a) physical meaning; (b) Force and displacement vs time.  $\mu$  is the friction coefficient,  $T_{sl}$  is the friction force during gross slip,  $N$  is the normal load and  $k_t$  is the tangential contact stiffness.

- *Separation* occurs when the normal load becomes zero and the contact interfaces detach (not shown in Fig. 1). In that case, no tangential contact force is transmitted, but energy can still be dissipated due to impacts between the interfaces.

It is important to accurately predict these contact states, as they strongly affect the structural dynamic response in terms of both stiffness and damping. For example, the higher the amplitude of slipping, the greater the energy dissipated by the frictional force since the area of the loop increases, although the loss factor is not monotonic with amplitude, as measured in [67]. At the same time, an increase in the amplitude of slipping also reduces the apparent stiffness of the system and the linear relationship ( $T = k_t \cdot x$ ) does not hold anymore.

In this study, hysteresis loops were measured from the two different high-frequency friction rigs at Imperial College London (Imperial) [44] and Politecnico di Torino (PoliTO) [45], which are shown in Figs. 2 and 3 respectively. Only a short description of the rigs is provided here, and for more information the reader is referred to the above references. Although their setup is quite different, the general idea behind the measurement is similar. Both rigs are excited harmonically with a shaker and generate an oscillating sliding motion between two contacting specimens. In the Imperial rig, one specimen is clamped to a moving block (see moving mass and moving arm in Fig. 2). As vibration begins, the specimen rubs over another specimen clamped to a static block (see static arm in Fig. 2). The moving block is connected to the ground by means of two very flexible leaf springs that enable large horizontal displacements when the block is excited by the shaker. Also in the PoliTO rig, one specimen is clamped to a moving block connected to the ground by means of leaf springs (see mobile specimen support in Fig. 3). However, the second specimen is not clamped to a static block, but to a more flexible holder that enables a contact self-alignment of the specimen interfaces (see self-alignment specimen support in Fig. 3). In both rigs, the relative displacement between the specimens is measured with Laser Doppler Vibrometers (LDVs) pointing very close to the contact interfaces to minimise the bulk deformation compliance. The high accuracy of the LDVs enables to measure the relative displacement between the two specimens with up to 0.05  $\mu\text{m}$  accuracy. The tangential friction force transmitted at the contact is measured with dynamic load cells that connect the specimen holders to the ground. Specimens are held in contact by applying a normal load, with a pneumatic actuator in the Imperial rig and with dead

weights in the PoliTO rig. Table 1 summarises the operating regimes of the rigs. In addition to the slightly different operating ranges, the rigs present two main design differences leading to several advantages and measurement challenges discussed throughout the article:

- *Contact approach*: rigid alignment vs self-alignment. The Imperial rig employs a classic rigid body contact approach, in which one mobile specimen moves rigidly towards a restrained specimen, only along the pre-defined normal direction in this rig. By using this technique, the area of contact strongly relies on the tolerance of the specimen contact interfaces, which, if not perfectly parallel to each other, will most likely give a point/line contact as shown in Fig. 4a. To transform the initial point contact into a flat distributed contact, several hysteresis cycles are required until the point contact extends to surface contact due to wear (see Fig. 4b). This approach leads to easy mounting and assembly, but it requires high-tolerance interfaces to guarantee a fully distributed flat contact, at least at the beginning of the test. If high-tolerance interfaces are not achievable, a certain running-in is required to establish a distributed contact. In contrast, the PoliTO rig uses a self-alignment system for the specimens, which avoids the possibility of point or line contacts. Self-alignment is achieved by introducing two additional degrees of freedom (rotations) as shown in Fig. 4c-e. In this case, the specimens are self-adjusting to each other as long as contact occurs on at least three points that define the contact plane (a detailed description of this mechanism can be found in [45]). A disadvantage of this contact approach is that the mounting procedure is more challenging and time-consuming than the procedure of a rigid approach. By nature, this system also provides more mounting flexibility, which can make an accurate stiffness measurement more challenging.
- *Contact geometry*: one-leg contact vs two-leg contact. Because of the self-aligning system, PoliTO specimens employ a two-leg contact interface, as shown in Fig. 3d to ensure stability, while the Imperial rig employs a simpler one-patch square contact interface, as shown in Fig. 2b. Both contacts are nominally flat in this study.

### 3. Round robin test description

A large test matrix was designed to record hysteresis loops at room temperature for a wide range of test conditions. The test matrix is

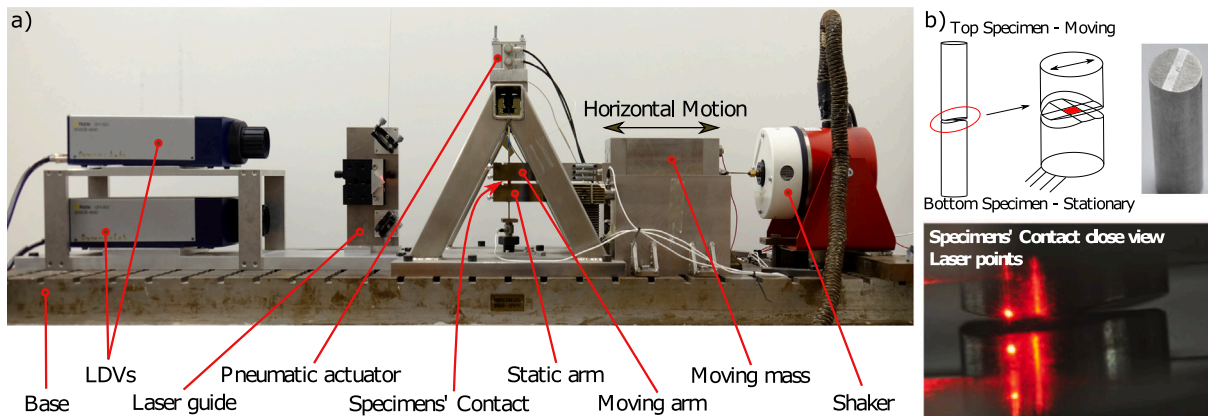


Fig. 2. (a) Imperial friction rig [14]; (b) Imperial specimens: one-patch square contact.

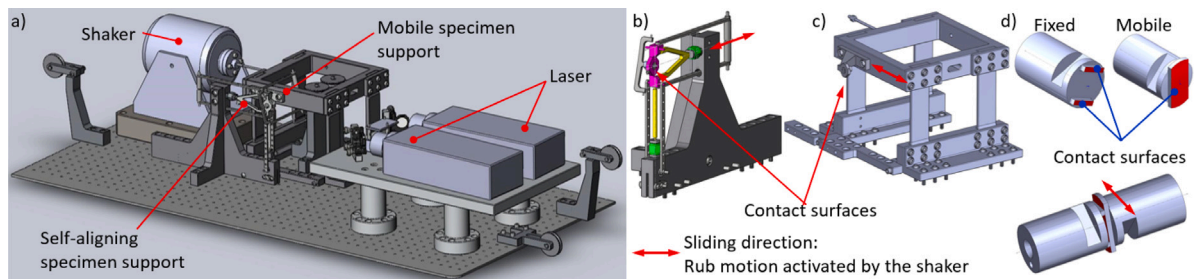


Fig. 3. PoliTO friction rig [45]: (a) overall view; (b) floating self-aligning specimen support; (c) mobile specimen support excited by means of the shaker; (d) PoliTO specimens: contact occurs on the two legs.

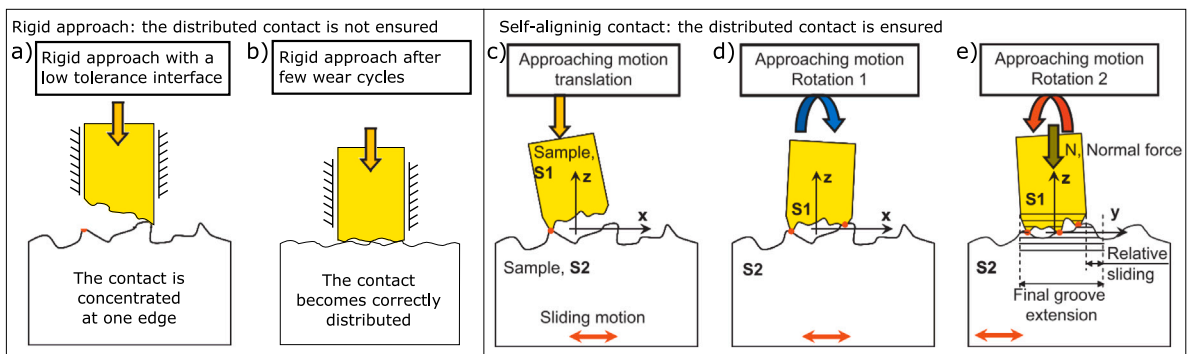


Fig. 4. (a–b) Rigid body contact approach of Imperial rig; (c–e) Self-aligning contact approach of PoliTO rig [45].

Table 1

Operating regimes of Imperial and PoliTO friction rigs.

	Imperial	PoliTO
Operating frequency	100 Hz	175 Hz
Displacement amplitude pk-pk at the operating frequency	0.5–25 $\mu\text{m}$	0.5–50 $\mu\text{m}$
Nominal contact area	1–25 $\text{mm}^2$	5–50 $\text{mm}^2$
Nominal contact pressure	Up to 500 MPa	Up to 50 MPa

shown in Fig. 5a, and consisted of four normal loads (17, 87, 150 and 253 N), four displacement amplitudes pk-pk (1, 14, 25 and 50  $\mu\text{m}$ ) and four nominal areas of contact (1, 5, 10 and 40  $\text{mm}^2$ ). In order to explore the widest possible experimental space and provide the largest set of data, each rig was tested at the extreme loading conditions that it could achieve. As a result, there was an overlap for 10 test conditions (circles with both green and red colours in Fig. 5a). The ranges of normal loads and displacement amplitudes were chosen to

measure hysteresis loops in all the different contact regimes, namely full stuck,<sup>2</sup> microslip and gross slip. The two rigs operate at slightly different excitation frequencies (100 Hz and 175 Hz), which correspond to the optimal excitation frequencies of each rig. A preliminary analysis was performed to investigate the effect of the excitation frequency on each rig. It highlighted that results were heavily dependent on the individual dynamic response of the rigs and hence it was decided to test at the optimal excitation frequencies only. Those excitation frequencies resulted in different peak sliding velocities of the specimens, obtained by multiplying the excitation frequency in [rad/s] by the pk-pk displacement amplitude divided by 2. To allow a comparison with similar sliding velocities, two of the displacement amplitudes were selected to

<sup>2</sup> A full stuck regime is never achievable in practice since a small part of the contact interface will always exhibit microslip. However, at very low displacement amplitudes, the portion of the interface in microslip is assumed to be negligible compared to the major remaining portion of the interface in a stuck condition.

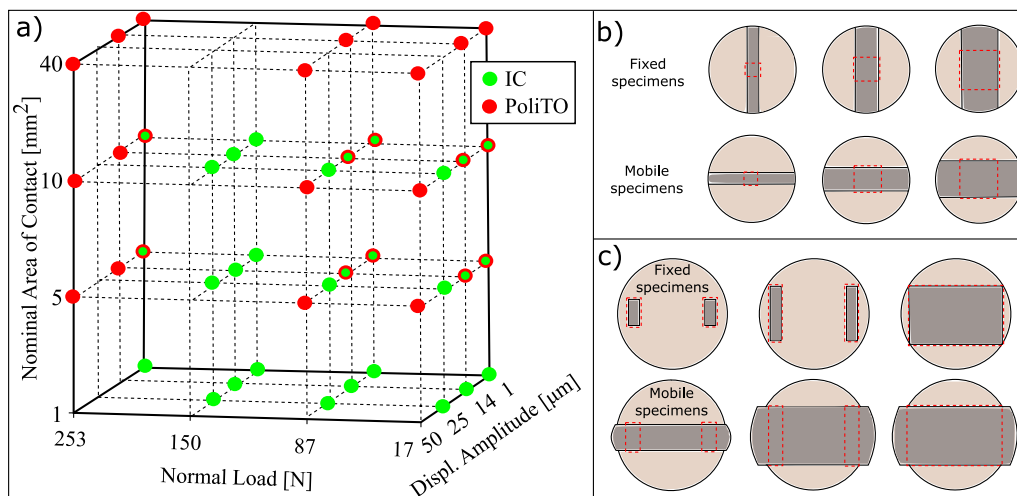


Fig. 5. (a) Test Matrix: tests with both colours were performed on both rigs; (b) Specimens of Imperial (from left to right 1 mm<sup>2</sup>, 5 mm<sup>2</sup> and 10 mm<sup>2</sup>); (c) Specimens of PoliTO (from left to right 5 mm<sup>2</sup>, 10 mm<sup>2</sup> and 40 mm<sup>2</sup>).

Table 2  
Test matrix summary.

	Units	Imperial	PoliTO
Material	–	Stainless steel 304	Stainless steel 304
Type of contact	–	Flat-on-flat (one leg)	Flat-on-flat (two legs)
Type of contact approach	–	Rigid body	Self-alignment
Temperature	–	Room temp.	Room temp.
Nominal areas of contact	[mm <sup>2</sup> ]	1/5/10	5/10/40
Normal loads	[N]	17/87/150/254	17/87/254
Min and max contact pressures	[MPa]	1.7–254	0.4–51
Excitation frequency	[Hz]	100	175
Displacement amplitudes pk-pk	[µm]	1/14/24.5	1/14/50
Peak sliding velocity	[mm/s]	0.31/4.40/7.70	0.55/7.70/27.5
Starting interface roughness	[µm]	0.5	5
Running time	[h]	2.5	2.5

provide the same peak velocity of 7.70 mm/s, resulting from 24.5 µm at 100 Hz for Imperial and 14 µm at 175 Hz for PoliTO, as shown in Table 2. In the designed test matrix, the lowest achievable velocity was 0.3 mm/s, which corresponds to the velocity of a stuck contact under a 100 Hz excitation.

The chosen range of nominal areas of contact was chosen to study the scalability of the results, but also to understand what is the best way of modelling frictional contacts in dynamics simulations (e.g. if it is better to discretise the interfaces with many 1 mm<sup>2</sup> contact patches or with fewer 40 mm<sup>2</sup> patches).

For every test condition, a new unworn specimen pair was used. Specimens were manufactured from the same batch of raw 304 stainless steel to guarantee comparability of the material. Each test lasted 2.5 consecutive hours to achieve a proper running, which was previously shown to be adequate to achieve stable contact conditions [63]. This led to more than 1.5 million hysteresis loops per test. Before and after every test, scans of the contact interfaces were acquired with an Alicona Infinite Focus instrument at PoliTO and an Olympus LEXT<sup>®</sup> OLS5000 3D Laser Confocal Microscope at Imperial. In this way, the condition of each specimen interface could be visually assessed before the experiments to ensure that the interface did not have scratches or imperfections. In fact, although specimens were all manufactured from the same batch of material, two different local companies manufactured the individual specimens for each rig, resulting in slightly different contact surface topographies. In the case of Imperial, specimen interfaces were carefully hand-polished after the manufacturing by using two different grades of abrasive paper: first, 800 grit for coarse and bulk material removal and, then, 2500 grit for smooth and finer surface finish, leading to a roughness value  $R_a$  of about 0.5 µm. The hand polishing process led to slightly curved contact interfaces since material

got removed at the sides first due to the rubbing on the abrasive paper. An example interface is shown in the optical scan of Fig. 6a, showing a “bump” in the centre. Note that the z-axis is magnified and better shown with Fig. 6b by means of the profile of the interface. The curvature was quantified by an equivalent radius of 33.2 mm, which is relatively large compared to the small interface width of only 1 mm. The curvature results in a bump of about 4 µm height, thus negligible compared to the width but very repeatable in every specimen. Although negligible, the bump is very helpful for ensuring high repeatability in the experiments since it leads to an initial point contact at the centre of the interface at the beginning of the test (the specimen interfaces could be associated with two crossed cylinders of radius 33.2 mm). The curvature also allows for an easier alignment during the tests since the Imperial rig does not employ a self-alignment contact approach. After 2.5 h of testing, the large number of wear cycles leads to a fully distributed contact over the whole nominal contact interface, as shown in Fig. 6c. The extension of the wear at the interface was quantified through the Digital Surf Mountains<sup>®</sup> software, by selecting the black worn spots and evaluating their extension (as the worn spot in Fig. 6c).

In the case of the PoliTO specimens, there was no manual sanding process introduced. The interfaces were provided by the manufacturer with a flat interface without any curvature and but they showed some machining marks that led to a larger initial roughness value  $R_a$  of 5 µm. A typical interface is shown in Fig. 7, where the machining marks are clearly visible outside the contact area while inside the contact area, on the location of the two legs of the mating specimen, a significant amount of material is missing due to wear. Although the initial roughness values are quite different between Imperial and PoliTO specimens, hysteresis measurements will show that the initial

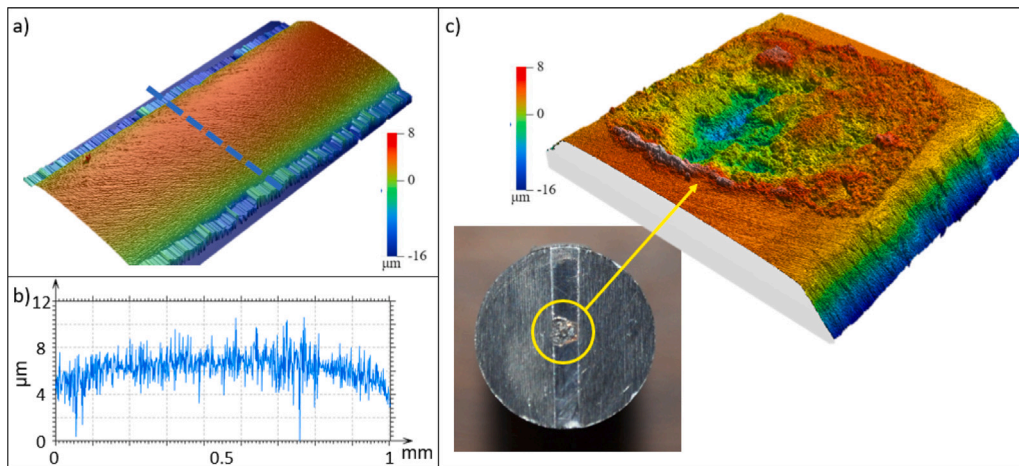


Fig. 6. (a) Scan of the unworn contact interface of an Imperial specimen; (b) Profile of the unworn contact interface; (c) Photo and scan of a fully worn contact interface of an Imperial specimen.

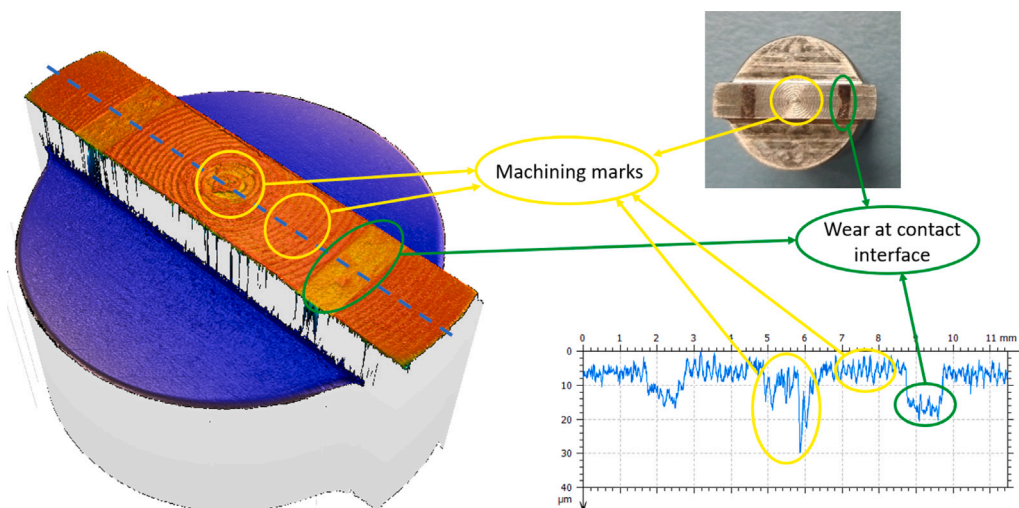


Fig. 7. Scan, photo and profile of the worn contact interface of a PoliTO specimen (the contact is on the two worn spots).

roughness wears away quickly during the early stage of the test resulting in very similar dynamic behaviour. This is evident in both Imperial and PoliTO specimens, from Figs. 6c and 7, where the amount of wear is of a much larger length scale than the initial roughness. Yet, different starting roughnesses could however affect the evolution of the contact parameters and interfaces until a steady state is reached, but this effect will be ignored at this stage.

### 3.1. Data post-processing

The large experimental matrix and the completion of all the tests resulted in more than 100 different specimen pairs being tested and more than 300 h of testing. At an average excitation frequency of 140 Hz, this corresponds to roughly 150 million hysteresis loops. Since recording all this data was unfeasible because of storage limits, loops were continuously recorded only during the first 5 s of each test. This was done because it was found that hysteresis loops strongly vary at the beginning of the test and consequently a high recording rate is needed to accurately capture their evolution [63]. After the first 5 s, loops were recorded with a lower rate until the 50th minute, after which only 10 consecutive hysteresis loops were recorded every 5 min. This procedure is reasonably chosen because, after a running-in, a steady state is slowly reached [63]. For every hysteresis loop, the following parameters were extracted:

- Friction coefficient,  $\mu$ , calculated with two methods, energy method and standard method, described in the Appendix A. Both methods were used in this research since some studies in the literature use only the first method and others only the second [36]. In this way, results could be compared to more studies.
- Tangential contact stiffness,  $k_t$ , calculated as the gradient of the stick portion of the loop from the reversal up until the force is equal to zero, as described in the Appendix A.
- Dissipated energy,  $E_d$ , evaluated as the area inside the hysteresis loop, i.e. the integral of the friction force over the relative displacement. The cumulative dissipated energy is obtained by summing up the energy dissipated by each loop during a test (assuming that the hysteresis loops not recorded dissipated the same energy as the latest available loop recorded). This energy enables a comparison of the results obtained under different test conditions (e.g. 1 h of testing performed at 24.5  $\mu\text{m}$  displacement amplitude would lead to more dissipated energy, and hence more wear, than a 1-hour test performed at 1  $\mu\text{m}$  of displacement amplitude).

The extraction was automated with the MATLAB<sup>®</sup> code described in the Appendix A, which processed each individual hysteresis loop and extracted automatically the contact parameters. The Appendix also shows a sensitivity analysis to assess the reliability and robustness of

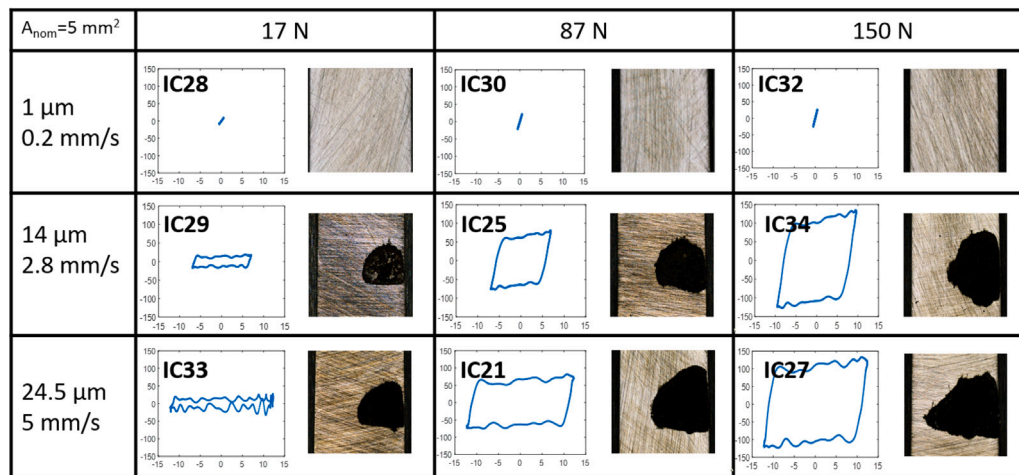


Fig. 8. Overview of contact interfaces and hysteresis loops for tests conducted on specimens with a  $5\text{ mm}^2$  nominal area of contact at Imperial. Columns are normal loads and rows are displacement amplitudes.

the post-processing technique, which is confirmed to be adequate and of much lower uncertainty than the inherent experimental uncertainty. Post-processing codes are available open access, with all experimental data, in [60].

#### 4. Measured hysteresis loops from the two friction rigs

Fig. 8 shows, as an example, the end-of-test contact interfaces and hysteresis loops for all the loading combinations of the specimens with nominal areas of contact of  $5\text{ mm}^2$  for the Imperial rig (similar results were obtained for the other nominal areas of contact). Not surprisingly, hysteresis loops strongly change as the displacement amplitude increases (loops from the top row to bottom row), shifting from being stuck with no gross slip at  $1\text{ }\mu\text{m}$  to established gross slip at  $14$  and  $24.5\text{ }\mu\text{m}$ . The normal load also strongly affects the shape of the hysteresis loops (columns from left to right) as would be expected. For loops in gross slip, the friction limit,  $\mu\text{N}$ , increases with the normal load. For fully stuck loops, the gradient increases with the normal load highlighting that the contact stiffness (which is obtained from the gradient) is normal load dependent, as already known in the literature [12,21,46,68]. At the very low normal loads of  $17\text{ N}$ , loops that are in gross slip show a large number of oscillations and appear to be quite noisy. These oscillations are due to a chattering phenomenon, which occurs when the normal load is so low that specimens are more prone to lift-off. At the larger  $150\text{ N}$  normal load, this effect disappears entirely since the chatter is suppressed. Another feature present in most of the hysteresis loops is the increasing friction force observed during the gross slip stage, as opposed to the expected constant Amontons-Coulomb friction force. In a previous study [65], this behaviour has been attributed to local wear scar interaction effects during the reciprocating sliding (e.g. interference of local interlocking peaks and troughs on the worn surfaces), but its true nature is still not well understood.

Fig. 8 also shows the contact interfaces at the end of each test. In the stick tests with  $1\text{ }\mu\text{m}$  relative displacement, the interfaces do not show any visible wear mark, suggesting that a negligible amount of energy has been dissipated during the test. At larger sliding distances, black wear scars appear indicating that worn areas have developed. These worn areas are larger when the normal load is larger since each loop dissipates more energy at larger normal loads (due to the larger area inside the loop). Note that a full worn area of contact is not reached in the specimens with the  $5\text{ mm}^2$  or the  $9\text{ mm}^2$  nominal area of contact, although it was reached in those with the lowest  $1\text{ mm}^2$  nominal area (not shown here for brevity). Longer tests would have been required to dissipate more energy and thus wear out interface material to a larger extent. This, however, was not the main scope of the round robin

test campaign and did not affect the analysis to a large extent since measured contact parameters were normalised by the real worn contact area as discussed in the following sections.

As for the PoliTO rig, Fig. 9 shows the end-of-test contact interfaces and the end-of-test hysteresis loops for all the loading combinations of specimens with nominal areas of contact of  $5\text{ mm}^2$ . Once more the hysteresis loops strongly change as displacement amplitude and normal load vary, in the same way as already observed with Imperial measurements. The main difference with Imperial measurements is that chattering does not appear during the PoliTO measurements and hence the loops are much smoother. This probably occurs because the “static” support of the PoliTO rig is flexible due to the self-aligning contact approach and hence it does not induce high-frequency vibrations due to its lower rigidity. Fig. 9 also shows the contact interfaces at the end of each test. In the stick tests at  $1\text{ }\mu\text{m}$ , the interfaces do not show any visible wear mark, suggesting that a negligible amount of energy is dissipated during the full stick regime. At larger sliding distances, coloured spots appear indicating that worn areas have developed. For the PoliTO specimens, fully extended worn areas are almost always reached in the  $5\text{ mm}^2$  tests and also some of the tests at larger nominal areas of contact ( $10$  and  $40\text{ mm}^2$ , not shown here for brevity). This probably occurs thanks to the self-aligning system, which guarantees a more uniform contact to start with and leads to higher wear rates. In addition, the PoliTO specimen interfaces do not show the curvature observed in Imperial specimen interfaces, thus leading to a more distributed and extended contact.

##### 4.1. Evolution of the contact parameters with wear

Results for a typical test on the Imperial rig are shown in Fig. 10a, which plots the evolution of the hysteresis loops over a test run. The hysteresis loops show a significant increase in the sliding friction limit,  $\mu\text{N}$ , as the test progressed. Since the normal load,  $N$ , remained constant during the whole test, this implies that the friction coefficient,  $\mu$ , has increased over time as the samples became worn. Fig. 10b shows the evolution of  $\mu$  as a function of the cumulative dissipated energy. The friction coefficient  $\mu$  rapidly increases within the first cycles from a very low value around  $0.1$ . This rapid increase matches previous observations [37,51,52,63,69,70] and it is attributed to the removal of initial oxide layers and contamination of the contact interfaces [71–74], which result in metal-to-metal contact and/or metal-to-wear particles contact that contribute to an increase in adhesion and ploughing. The steady state reached after approximately  $100\text{ J}$  of energy dissipated, has been attributed to a balance between the generation and ejection of wear debris from the contact interface [72].

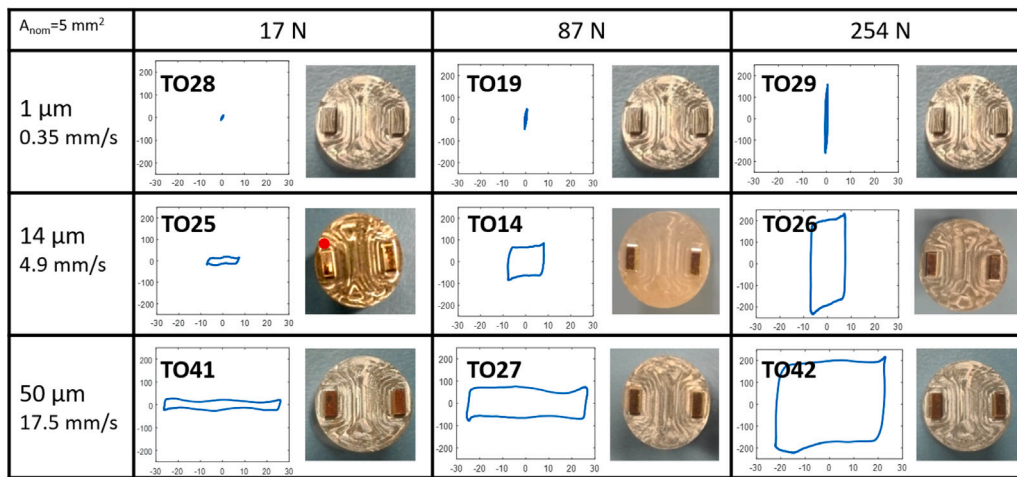


Fig. 9. Overview of contact interfaces and hysteresis loops for tests conducted on specimens with a 5 mm<sup>2</sup> nominal area of contact at PoliTO. Columns are normal loads and rows are displacement amplitudes. The red dot indicate the standard position of the laser measurement location since the displacement could only be measured on one of the two contact legs during the experiment.

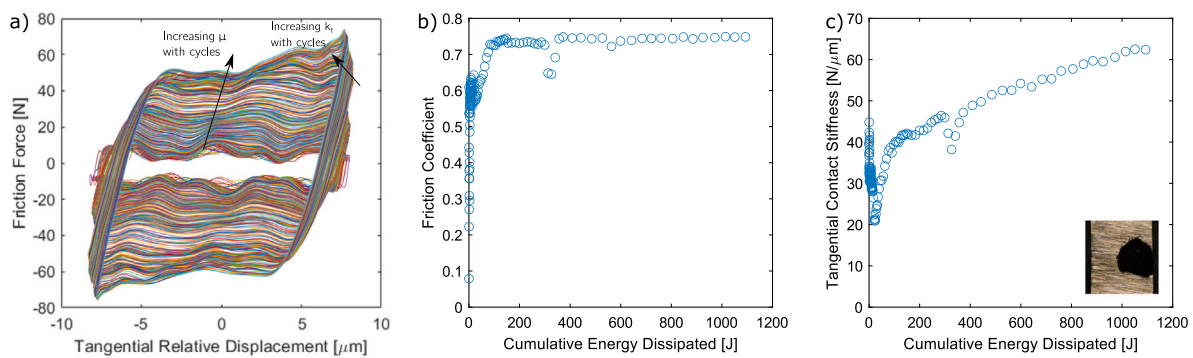


Fig. 10. Typical Imperial evolution of contact parameters: (a) Hysteresis loops; (b) Friction coefficient; (c) Tangential contact stiffness and worn area at the end of the test. Values for the Test n. IC25: 87 N normal load, 14 µm relative displacement, 5 mm<sup>2</sup> nominal area of contact, 100 Hz excitation frequency and 2.5 h of running, total hysteresis cycles = 900 000, material = stainless steel, temperature = 25 °C.

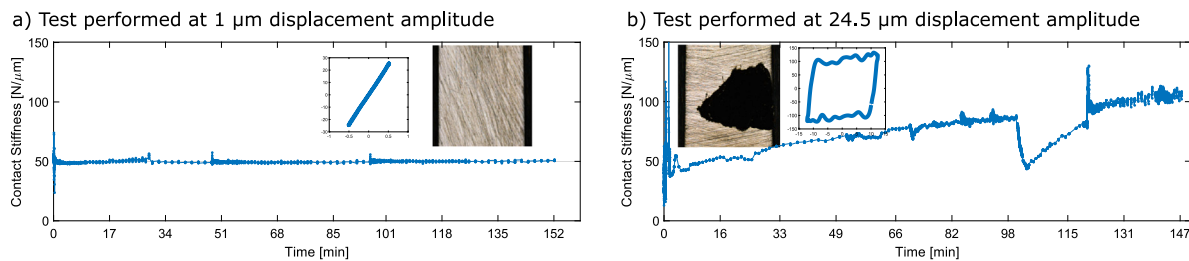


Fig. 11. Evolution of tangential contact stiffness: (a) Tests performed at 1 µm displacement amplitude; (b) Tests performed at 24.5 µm displacement amplitude. The interface photos show the worn areas of contact at the end of the test, and the hysteresis loops are the loops at the end of the tests. Values for the Tests n. IC32-27: 150 N normal load, 1 µm and 24.5 µm displacement amplitude respectively, 5 mm<sup>2</sup> nominal area of contact, 100 Hz excitation frequency and 2.5 h of running, total hysteresis cycles = 900 000, material = stainless steel, temperature = 25 °C.

Fig. 10c shows the trend of the tangential contact stiffness,  $k_t$ , which increases at a slower rate than  $\mu$ , without reaching a steady state in this particular test. This slow increase is probably due to the slow increase in the worn area of contact, which evolves from the initial point contact, due to the curved shape of a 4 µm bump shown in Fig. 6, to a more distributed contact at the end of the test. The removal of the bump with wear would in fact lead to a more conformal and less compliant contact with a higher final stiffness value. This hypothesis suggests that the steady state in the  $k_t$  should be reached when the area of contact reaches the maximum extension. For this reason, the  $k_t$  increasing rate is slower than that of  $\mu$ , since the worn area requires

more energy to evolve as compared to the lower energy required for the removal of the contaminated layer that leads to the  $\mu$  increase. To confirm this hypothesis, Fig. 11 shows two tests performed at different displacement amplitudes, 1 µm and 24.5 µm respectively, and their corresponding end-of-test contact interfaces. The test performed at 1 µm displacement amplitude does not show any sign of wear, due to the null amount of energy dissipation within the stuck loops, and indeed its  $k_t$  is constant during the whole test. Instead, the test performed at 24.5 µm displacement amplitude shows a clear increase in the  $k_t$  value associated with the increase in the worn area of contact due to the energy dissipated within the gross slip hysteresis loops (the drop

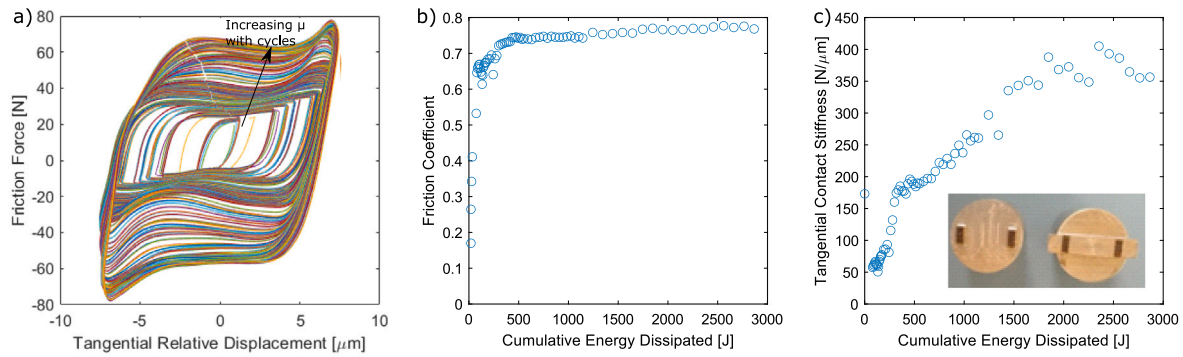


Fig. 12. Typical PoliTO evolution of contact parameters: (a) Hysteresis loops; (b) Friction coefficient; (c) Tangential contact stiffness and worn area at the end of the test. Values for the Test n. TO14: 87 N normal load, 14  $\mu\text{m}$  relative displacement, 5  $\text{mm}^2$  nominal area of contact, 175 Hz excitation frequency and 2.5 h of running, total hysteresis cycles = 1 575 000, material = stainless steel, temperature = 25  $^{\circ}\text{C}$ .

observed at about 320 J, after 98 min of testing, could be due to some temporary unbalance in the wear debris formation/ejection). The  $k_t$  value approaches an asymptote since the worn area of contact is almost fully extended (it is certainly more extended than that of the test in Fig. 10 where a steady state was not reached). Similar increases have also been observed in previous studies that measured the evolution of  $k_t$  with wear [46,63,70].

Similar trends in  $\mu$  and  $k_t$  were also observed in the PoliTO rig. Fig. 12 shows a typical PoliTO test performed under the same condition as the Imperial test of Fig. 10 with a 87 N normal load and 14  $\mu\text{m}$  relative displacement. The friction coefficient  $\mu$  rapidly increases at the beginning of the test, although it reaches the steady state after roughly 500 J dissipated, more than the Imperial 100 J. Also  $k_t$  increases but, contrary to what was observed on the Imperial rig, it seems to reach a steady state, which is attributed to the approach of the full worn area (as shown in the full worn specimen photo, in contrast with the Imperial specimen that has not a full worn contact). The full worn area for the PoliTO specimen was probably reached because of a flatter initial interface and the self-aligning system, which ensured full contact. In addition the larger excitation frequency led to more cycles in the 2.5 h and hence to more energy dissipated at the contact (the steady state is reached in PoliTO at around 1500 J of energy dissipated, while in Imperial the test stopped at 1100 J). It is important to notice that the PoliTO contact stiffness value is almost 7 times larger than that of Imperial. This mismatch only occurs because such stiffnesses are not normalised by the worn area of contact, which indeed is larger in PoliTO specimen, as better discussed in the following section.

## 5. Comparison of contact parameters from the two friction rigs

This section compares the post-processed measurements obtained from the two friction rigs, highlighting agreement and differences. First, measured  $k_t$  and  $\mu$  are compared and then the potential impact of the two rig design differences on the measured data is discussed.

### 5.1. Tangential contact stiffness, $k_t$

For each test, end-of-test values of  $k_t$  were calculated as described in the Appendix B, where supplementary plots are also shown with the exact values and standard deviations for every loading combination. Fig. 13 shows a qualitative summary of the  $k_t$  steady state values on both Imperial and PoliTO rigs (if a steady state was not reached, the end-of-test values were chosen instead). Several trends emerge from the results, which are discussed below.

#### 5.1.1. Effect of normal load and worn area of contact

Fig. 13 shows that  $k_t$  strongly increases with the normal load almost fourfold in Imperial tests, with values rising from about 25  $\text{N}/\mu\text{m}$  to 90  $\text{N}/\mu\text{m}$  when the normal load increases from 17 N to 150 N. In the case of the PoliTO tests, the normal load dependence is even stronger with values rising from as low as 25  $\text{N}/\mu\text{m}$  to 2000  $\text{N}/\mu\text{m}$  when the normal load increases from 17 N to 254 N. This increase of  $k_t$  with the normal load is well known and has already been observed in a range of experiments [12,21,46,68], being attributed to the increase in the number and size of the individual contact spots, resulting in a larger real area of contact and more interactions of asperities at the interface [68]. The absolute increase observed in the PoliTO tests is much larger than the increase observed in Imperial tests and it is here attributed to the much larger worn areas of contact observed in PoliTO specimens, which reach up to 40  $\text{mm}^2$  compared to the maximum 2.5  $\text{mm}^2$  in the Imperial case.

Since the worn area of contact leads to larger stiffnesses,  $k_t$  values from Fig. 13a–d were normalised by the measured worn area of contact of each specimen after test, thus obtaining normalised tangential contact stiffness values,  $K_T$ , expressed in  $\text{N}/\mu\text{m}/\text{mm}^2$  (different from the small letters  $k_t$ , expressed in  $\text{N}/\mu\text{m}$ ). It is common practice to normalise contact stiffness against the nominal contact area [4,75], but since the actual worn contact area could be measured for these tests, it was considered a more appropriate normalisation parameter. Fig. 13b–e plots the worn area normalised  $K_T$  for Imperial and PoliTO, while the values of worn areas of contact are shown in Figs. 13c–f. Note that the 1  $\mu\text{m}$  tests did not show any wear due to a negligible amount of energy being dissipated in stuck loops. Therefore, to get the normalised  $K_T$  for those cases, the following procedure was performed: at the end of each test with a 14  $\mu\text{m}$  displacement amplitude, the hysteresis loop was brought down to a 1  $\mu\text{m}$  displacement amplitude and the  $k_t$  was extracted. In this fully-worn case, it was possible to measure  $k_t$  at 1  $\mu\text{m}$  displacement amplitude but on specimens with a fully developed worn area of contact. The normalised  $K_T$  in Fig. 13b at 1  $\mu\text{m}$  was obtained in this way. Fig. 13b–e show that the normal load dependency still holds, with normalised  $K_T$  values in the range 20–80  $\text{N}/\mu\text{m}/\text{mm}^2$  at Imperial and 10–250  $\text{N}/\mu\text{m}/\text{mm}^2$  at PoliTO. To make the tangential stiffness values from the two rigs truly comparable, the applied normal load was divided by the worn area of contact leading to a comparison of the normalised stiffness over the applied contact pressures. The final results of the comparison are shown in Fig. 14, which shows a quite clear increasing trend with most PoliTO tests overlapping with Imperial tests, except a few PoliTO tests that show much larger values. The large discrepancy is probably due to the following reasons:

- PoliTO  $k_t$  estimations are expected to be slightly larger because of the different contact surface topographies with respect to Imperial specimens. Imperial specimen interfaces have a slight curvature that increases the compliance, while PoliTO specimens are flat-on-flat and, thus, expected to be stiffer.

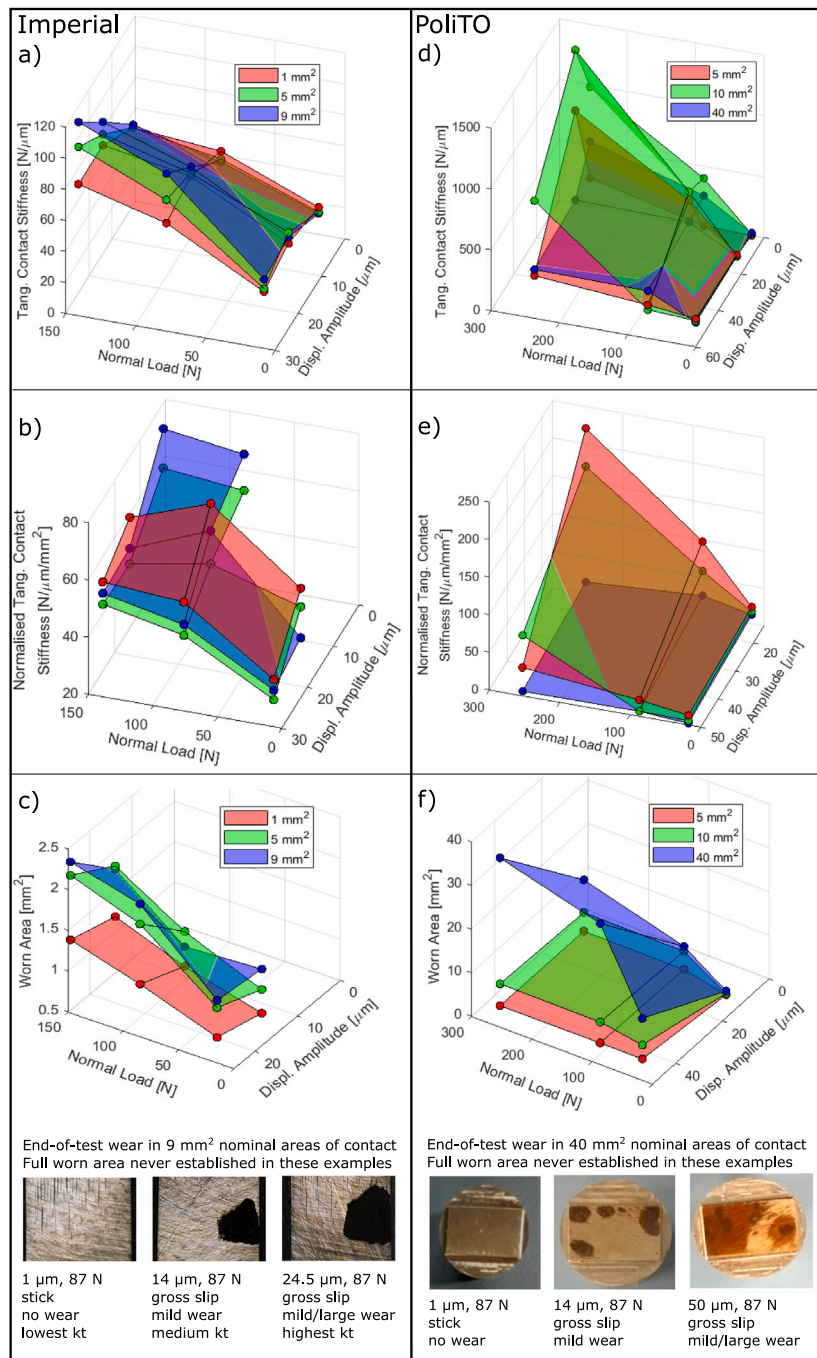


**Fig. 13.** Tangential contact stiffness steady state values,  $k_t$ , for the (a) Imperial and (d) PoliTO friction rigs; Worn area normalised tangential contact stiffness steady state values,  $K_T$ , for the (b) Imperial and (e) PoliTO friction rigs; Worn areas of contact at the end of each test, plus example photos of worn areas at the end of tests, for the (c) Imperial and (f) PoliTO friction rigs.

- $k_t$  estimations above 300 N/μm are less reliable due to the very small relative displacements measured by the laser. In those cases, even minimal changes in the measured displacement lead to major changes in the  $k_t$  estimated from the force–displacement slope. Indeed, the four outliers in Fig. 14a resulted from  $k_t$  values above 500 N/μm (see Fig. 14b), which result from corresponding displacements in the stick portion of the loop below 0.05 μm, which are difficult to accurately measure and strongly affect the  $k_t$  estimation even for small deviations.
- The two friction rigs have quite different designs and, in addition, the  $k_t$  experimental uncertainty was in the range of 25% for Imperial and 60% for PoliTO estimated through a series of

repeatability tests performed by assembling and disassembling the same specimen pair several times and testing it under the same loading conditions.

If the two PoliTO outliers are excluded, the load dependency of the tangential contact stiffness can be represented by a square fit of  $K_T$  versus the worn-area-normalised normal load ( $K_T = K_1 * p^{\frac{1}{2}} = 6.3 * p^{\frac{1}{2}}$ ). The coefficient  $K_1$  is equal to 6.3, obtained by fitting the experimental data, and gives a stiffness in N/μm/mm<sup>2</sup> when multiplied by the square root of the normal load divided by the worn area,  $p$ , expressed in MPa. Note that, although many experiments were performed under the same normal loads, they show different pressures since normal loads are normalised by the worn areas of contact, which differ test by test.

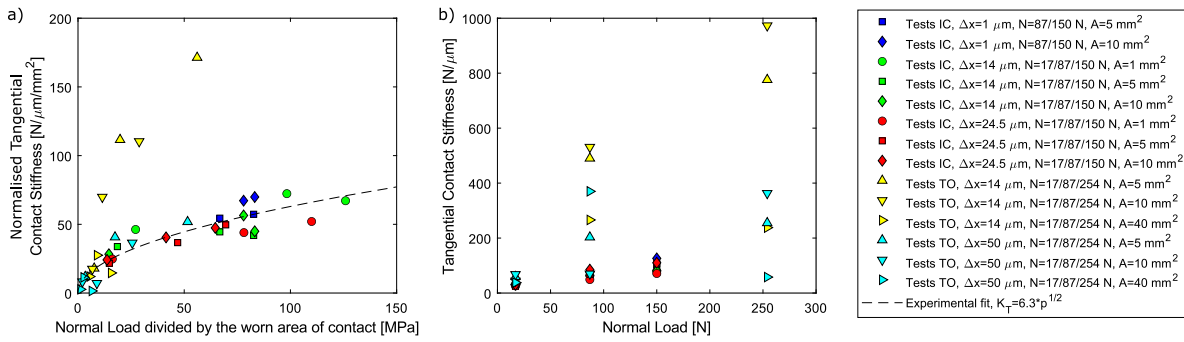


**Fig. 14.** Tangential contact stiffness steady state values. Each point in the Figure corresponds to a different test of the round robin matrix with a different worn area of contact: (a) Worn area normalised  $K_T$  versus contact pressure (normal load divided by the worn area). Note that, although some tests were performed with the same normal load, they have different contact pressures due to their different worn areas. The experimental fit on the Imperial tests is also shown; (b) Un-normalised  $k_t$  versus normal load.

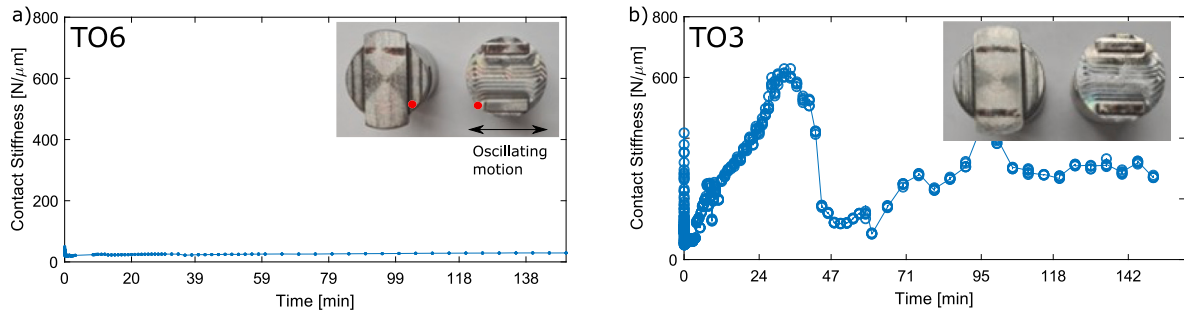


**Fig. 15.** Evolution of the tangential contact stiffness of two tests performed on the PoliTO friction rig under the same loading conditions (87 N normal load, 14 μm displacement amplitude, 10 mm<sup>2</sup> nominal area of contact): (a) Test n. TO6,  $k_t$  is very low because the displacement is measured on the leg not in contact (see red dot); (b) Test n. TO3,  $k_t$  is larger because the contact is concentrated on the measured leg too.

Larger worn areas of contact lead in fact to lower pressures and hence different normalised  $k_t$  values.

The exact values and standard deviations for every loading combination across all the measured specimens are shown in the [Appendix B](#) through violin plots. The relative standard deviation of the steady state values within the individual tests is below 10% at Imperial, except for the test performed at 17 N that showed the chattering phenomenon. In the case of the PoliTO tests, the relative standard deviation of the steady state values within the individual tests is below 8% for tests with low  $k_t$  values, while the relative standard deviation increases up to the 40% for tests with very large  $k_t$  values, over 300 N/μm, because of the very low measured displacements.

### 5.1.2. Effect of the distribution of the worn area of contact

The extension of the worn area of contact is not the only driving parameter for the  $k_t$  estimation, which indeed seems to be also driven by the spatial distribution of the wear spots over the contact [4,76]. The effect of the spatial distribution is explained and clarified here with two tests. [Fig. 15a](#) represents an extreme case in which one leg was not in contact at all due to an improper assembly of the specimens. The  $k_t$  measured in this test is very low (below 20 N/μm) if compared to the  $k_t$  from test in [Fig. 15b](#), which was performed under the same loading conditions but with the contact distributed on both legs. The red dots in [Fig. 15a](#) indicate the location of the laser measurement. Due to the one-sided contact, the specimen was rotating around the leg in contact, while the displacement was measured on the opposite unsupported leg. As a result, a large displacement was measured, leading to much lower  $k_t$  estimations.

This example highlights that  $k_t$  estimations are strongly dependent on the kinematics of the contacting components and hence that it is important to accurately choose the most representative laser measurement locations for reliable  $k_t$  estimations. The displacement needs to be measured as close as possible to the actual spots of contact, which

can be distributed in different locations if the nominal area is wide. Ultimately, the kinematic behaviour depends on where the interfaces get into contact, as demonstrated on more complex structures [4]. In other words, it strongly depends on the spatial contact distribution, namely the pressure distribution. The importance of the spatial contact distribution, and not only of the overall extension, has been observed experimentally in the pioneering work of Kendall and Tabor [68], who described the effect of the position of contact spots on the  $k_t$  estimations (i.e. contacts of the same size close to each other lead to lower  $k_t$  than contact spots further away from each other). The effect of the contact spots spacing has also been modelled numerically [61]. However, to the best of the authors' knowledge, such observations are missing in more recent experimental studies despite this being an important piece of information if an accurate measurement of  $k_t$  is required.

### 5.1.3. Effect of displacement amplitude

[Fig. 13a–d](#) showed unclear trends of  $k_t$  with the displacement amplitude due to the different worn areas of contact at different displacement amplitudes. Therefore, [Fig. 13b–e](#) is analysed since it shows the  $K_T$  normalised by the worn areas of contact. For both Imperial and PoliTO, the normalised  $K_T$  decreases as the displacement amplitude increases. This behaviour has been confirmed by performing an additional experiment at the standard normal load of the round robin, 87 N, with a 30 μm and 1 mm<sup>2</sup> nominal area of contact at Imperial and 50 μm and 10 mm<sup>2</sup> nominal area of contact at PoliTO. After reaching the steady state with a fully worn area of contact, several hysteresis loops were recorded at different displacement amplitudes as shown in [Fig. 16a–c](#). The corresponding  $k_t$  estimations from both rigs are shown in [Fig. 16b–d](#) as a function of the displacement amplitude. The displacement dependency is clear, with  $k_t$  values reducing approximately by 60% over the thirtyfold increase in displacement amplitude at Imperial, nearly reaching an asymptote at the largest tested amplitude, and reducing by 5 times over the sixtyfold increase in displacement amplitude at PoliTO,

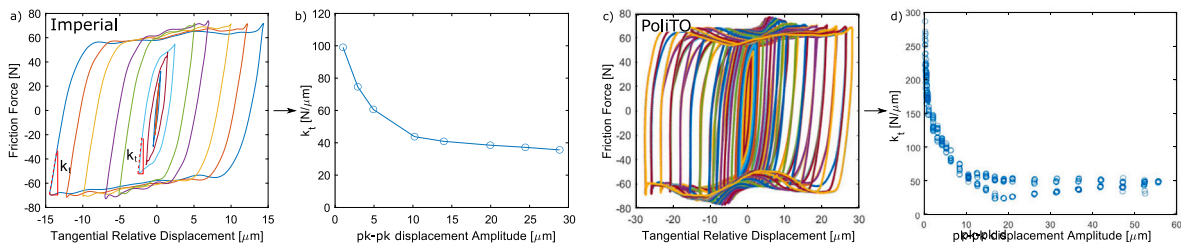


**Fig. 16.** (a) Hysteresis loops measured at different displacement amplitudes within the same test (a) Imperial rig at 100 Hz excitation frequency and (c) PoliTO rig at 175 Hz excitation frequency; (b–d)  $k_t$  as a function of the displacement amplitude from hysteresis loops shown in (a–c). Note that  $k_t$  is the slope measured right after the load reversal in each hysteresis loop. Test conditions: 87 N normal load, 1 and 10 mm<sup>2</sup> nominal areas of contact at Imperial and PoliTO respectively, steady state reached after 2.5 h of running at 30 and 50 μm displacement amplitudes at Imperial and PoliTO respectively, and then loops measured at different displacement amplitudes, material = stainless steel, room temperature.

reaching a clear asymptote over 20 μm. Measurements were performed with both increasing and decreasing displacement amplitudes and the trend was repeatable in both loading directions. As a reminder, the  $k_t$  values represent the  $k_t$  estimated right after the load reversal obtained by fitting the only stick region. The drop in the  $k_t$  (evaluated after load reversal) with the increasing displacement amplitude has been observed in a few previous studies [25,53,63,77].

One possible physical explanation for this behaviour was provided in [13] based on an ultrasonic investigation performed on the Imperial rig. The  $k_t$  displacement dependency was linked to the ageing phenomenon at the interface. Ageing results from the time of stationary contact during which the junction size at the asperity contact increases, induced by asperity creep and strengthening of bonding at asperity contacts [34,78–80] and hence the area-dependent stiffness increases as well. Optical measurements have already shown how the real area of contact slowly increases, typically logarithmically, with the time spent in contact, at rest, due to the ageing or contact rejuvenation [18,81]. This concept can be applied to the present measurements by assuming that the stick condition is equivalent to a period of stationary resting contact. The ageing would lead to increased stiffness values during repeated stick cycles at low displacement amplitudes, and hence quasi-stationary contact with a very low relative velocity. Instead, at large displacement amplitudes, the asperities would be in stick conditions for shorter periods, thus reducing the amount of ageing and consequently resulting in lower contact stiffness. Once gross slip is reached, the contact would reset and ageing would have to restart at the next stick condition. This hypothesis is well supported by the ultrasound measurements shown in [13], and the results shown here may further support this hypothesis. The PoliTO results in Fig. 16 show that the  $k_t$  stops decreasing after a certain threshold, namely 20 μm pk-pk displacement amplitude, which corresponds to roughly 11.0 mm/s peak velocity at 175 Hz. It seems therefore that no ageing occurs at velocities larger than 11.0 mm/s probably because, above those velocities, the rate of change of the contacting asperities overcomes the time required for them to age. The maximum peak velocity achieved in the Imperial test is instead 9.4 mm/s and the asymptote is not clearly stabilised. Probably, also in Imperial specimens the limit velocity to reach the asymptote is around 10–11 mm/s. More quantitative analyses will be performed in the future to confirm this hypothesis and understand what are the parameters that affect this threshold, such as supposedly the size of the asperities and the tendency to creep of the particular material.

In addition, or as an alternative to the ageing hypothesis, the drop in stiffness could also be caused by the increase in energy dissipation at larger velocities, which may lead to a rise in the contact interface temperature. This temperature increase could potentially lead to more compliance in the interface, and hence a drop in the tangential contact stiffness. To investigate this further, temperature measurements were taken for the PoliTO specimens with thermocouples embedded in the specimens 1 mm away from the contact interface. Measurements showed relatively low temperatures, below 50 °C, in agreement with previous studies [49,82]. This low temperature does not support this

second hypothesis, although it is known that flash temperatures at the asperity contacts can reach much higher values (>500 °C) [82,83], which cool very quickly some mm far from the contact in the bulk material, where the temperature was indeed measured in the presented experiments.

#### 5.1.4. Effect of plastic hardening in fully stuck tests

Table 3 compares the end-of-test values for both Imperial and PoliTO tests performed at 1 μm of displacement amplitude. At 17 N normal load,  $k_t$  values are below 30 N/μm, for both the nominal areas of 5 and 10 mm<sup>2</sup>. Also for the 87 N case and 5 mm<sup>2</sup>, the  $k_t$  estimations are relatively close, below 45 N/μm. However, the Test TO10 performed at 87 N normal load and 10 mm<sup>2</sup> nominal area shows a  $k_t$  value extremely large, 578 N/μm. The reason for this very large value is that the PoliTO  $k_t$  increased during the 1 μm test as shown in Fig. 17b. This increase might be attributable to the small amount of energy being dissipated during the test, shown by the non-zero area inside the loops in Fig. 17a despite the very low displacement amplitude of 1 μm. This amount of energy dissipated is not large enough to generate a worn area at the end of the test, as shown by the pristine area in Fig. 17b, but it is large enough to lead to an increase in the  $k_t$ , which reaches a “steady state” after 22 J low amount of energy dissipated. It is hypothesised here that this energy led to a plastic hardening of the asperities, which dissipate some energy during microslip loading and unloading cycles, hence increasing the stiffness of the contact and resulting in larger  $k_t$  estimations.

Instead, Imperial hysteresis loops did not show any evolution in the  $k_t$  values during the whole tests since they were almost straight lines without any apparent microslip or energy dissipation, see e.g. Fig. 11a at 1 μm. The reason why 1 μm displacement loops at PoliTO dissipate more energy than loops at Imperial is that the PoliTO loops have larger initial  $k_t$  values (around 300 N/μm) compared to those observed in Imperial stuck tests (around 50 N/μm), probably due to the hertzian contact in Imperial compared to the flatter contact in PoliTO. For this reason, larger tangential loads are reached with lower displacement amplitudes, thus increasing the possibility to encounter microslip even at low displacement amplitudes such as 1 μm. It is thus concluded that stick tests performed at 1 μm displacement amplitude are very comparable between Imperial and PoliTO, except in cases where microslip is present, which leads to the energy dissipated with consequent increases in the  $k_t$  values. As a result, it is suggested to maintain displacement amplitudes as small as possible when measuring stuck hysteresis loops to avoid any potential microslip that may lead to significant increases in  $k_t$ , possibly due to plastic hardening.

#### 5.2. Friction coefficient, $\mu$

The friction coefficient was extracted from the hysteresis loops with two methods, the energy method and the standard method, as described in the Appendix A. Then, the steady state values were calculated for each test as described in the Appendix B, which in general were reached

**Table 3**

Steady state  $k_t$  values for the 5 and 10 mm<sup>2</sup> nominal areas of contact performed at 1  $\mu\text{m}$  of displacement amplitude, and 17 N and 87 N normal loads.  $E_{kt}$  indicates the energy dissipated when a steady state in the  $k_t$  was reached. No one test presented any amount of wear.

Measurements at 1 $\mu\text{m}$ displacement amplitude	17 N		87 N	
	Imperial	PoliTO	Imperial	PoliTO
$A_{nom} = 5 \text{ mm}^2$	Test IC28 $k_t = 17 \text{ N}/\mu\text{m}$ $E_{kt} = 0.0 \text{ J}$	Test TO28 $k_t = 14 \text{ N}/\mu\text{m}$ $E_{kt} = 0.0 \text{ J}$	Test IC30 $k_t = 42 \text{ N}/\mu\text{m}$ $E_{kt} = 0.2 \text{ J}$	Test TO19 $k_t = 24 \text{ N}/\mu\text{m}$ $E_{kt} = 0.1 \text{ J}$
$A_{nom} = 10 \text{ mm}^2$	Test IC17 $k_t = 16 \text{ N}/\mu\text{m}$ $E_{kt} = 0.0 \text{ J}$	Test TO24 $k_t = 27 \text{ N}/\mu\text{m}$ $E_{kt} = 1.4 \text{ J}$	Test IC23 $k_t = 39 \text{ N}/\mu\text{m}$ $E_{kt} = 0.0 \text{ J}$	Test TO10 $k_t = 578 \text{ N}/\mu\text{m}$ $E_{kt} = 22 \text{ J}$

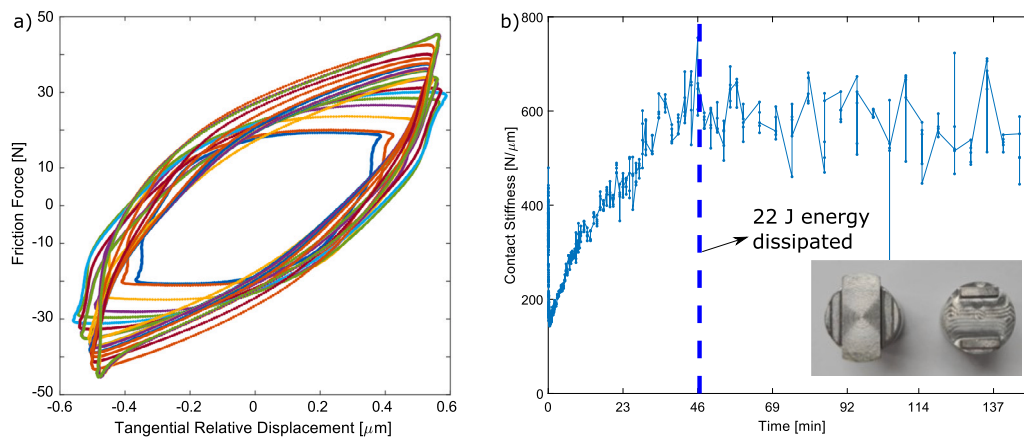


**Fig. 17.** (a) Evolution of hysteresis loops for the Test n. TO10 performed at 1  $\mu\text{m}$  displacement amplitude on the PoliTO friction rig; (b)  $k_t$  evolution in time. The photo shows the specimen interfaces at the end of the test (no wear present). The vertical line indicates the beginning of the steady state. Values for the Test n. TO10: 87 N normal load, 1  $\mu\text{m}$  displacement amplitude, 5 mm<sup>2</sup> nominal area of contact, 175 Hz excitation frequency and 2.5 h of running.

within the first 15 min quite consistently. Fig. 18a–b shows the  $\mu$  steady state values for the Imperial and PoliTO rigs calculated with the standard method. Only the standard method estimations are shown since, in the case of Imperial, standard and energy methods led to the same  $\mu$  values. In the case of PoliTO, estimations for the two methods were slightly different, with standard  $\mu$  estimations being on average 6% higher than energy  $\mu$  estimations. This occurs because the microslip region in PoliTO tests is much more dominant than in Imperial tests, where instead the transition from stick to gross slip is sharper. The sharper the transition, the larger the energy  $\mu$  estimations. A hysteresis loop with a sudden transition from stick to gross slip would have the same values of energy and standard  $\mu$ . If a microslip transition state existed, the energy dissipated would have been lower, thus leading to a lower energy  $\mu$  estimation, whilst maintaining the same standard  $\mu$  estimation. More details on the differences between different  $\mu$  estimation techniques can be found in the following review [36].

Fig. 18c shows the comparison of standard  $\mu$  values plotted versus the normal load. A decreasing trend of  $\mu$  with respect to the normal load is visible, especially in the PoliTO rig where the average  $\mu$  values and relative standard deviations are equal to 1.04 (14.2% std) at 17 N, 0.78 (3.0% std) at 87 N and 0.75 (6.9% std) at 254 N, while the Imperial values slightly decrease from 0.77 at 17 N to 0.72 at 150 N. The reason for this observed decrease is not clear yet and could be attributed to the fact that, at larger normal loads, a fully established gross slip could not have been achieved within the relatively small investigated displacement amplitudes (14  $\mu\text{m}$  and 50  $\mu\text{m}$ ). In addition, measurements at the lower 17 N normal loads are in general less reliable. If compared to the Imperial 0.77 average  $\mu$  at 17 N normal load, the PoliTO  $\mu$  values are much larger, up to 1.24. This relatively large difference of 35% is not attributable to the repeatability of the measurements, whose uncertainty was quantified to be below 4% for Imperial tests and below 8% for PoliTO tests performed under the same loading conditions.

Instead, the difference is here attributed to the very low conformity resulting from such low loading, which leads to more unstable and less reliable hysteresis loops as the chattering phenomenon may occur. In addition, at low normal loads, some inaccuracies might also appear in the normal load measurement. While the normal load is easy to check in the PoliTO rig since it is applied employing dead weights of known mass, in the case of the Imperial rig it is applied by means of a pneumatic actuator and measured with a strain gauged load cell. The strain gauge load cell could be inaccurate at low normal loads and this could be another reason for the observed differences. For all of the above reasons, it is concluded that measurements of the friction coefficient should be performed at normal loads large enough to guarantee adequate conformity that does not lead to separation phenomena, such as chattering and other instability effects.

The effects of different displacement amplitudes and nominal areas of contact on the extracted friction coefficients in Fig. 18a–b are less obvious, suggesting that these parameters do not affect  $\mu$  estimations to a large extent. All the extracted steady state  $\mu$  values and standard deviations can be found in the Appendix B.

Finally, with regards to the evolution with wear, it was observed that the energy dissipated to reach a steady state was, in general, comparable between Imperial and PoliTO (in the range 100–1000 J), see e.g. the evolution in Figs. 10b and 12b, or the Figures in the Appendix B. Reaching steady states required more energy dissipation in tests performed at larger normal loads than in tests performed at lower normal loads. A possible hypothesis for this behaviour is that, at lower normal loads, the wear particles of the original oxide layer are ejected more easily from the contact and thus less energy dissipation is required to reach steady state. It is recommended that the evolution of the friction coefficient is closely monitored during testing, especially in the first cycles, to ensure that steady state values are extracted.

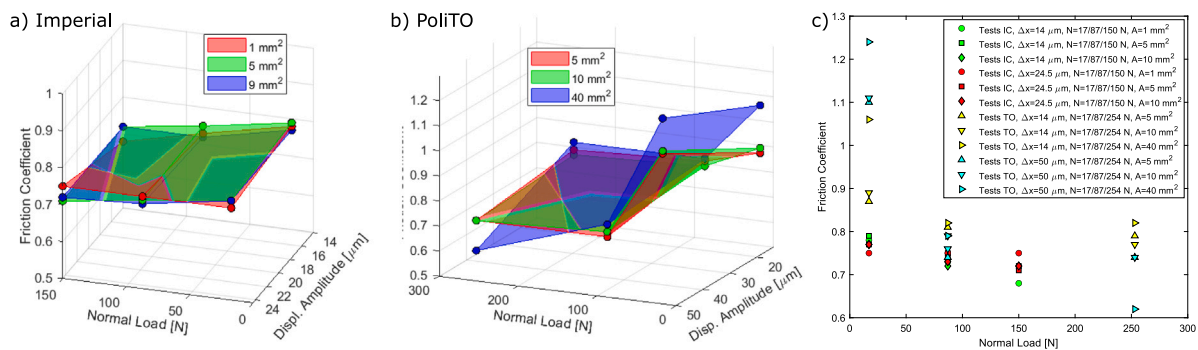


Fig. 18. Friction coefficient steady state values of the round robin test on the (a) Imperial and (b) PoliTO friction rigs. (c) Friction coefficient steady state values plotted versus the normal load. Each point in the Figure corresponds to a different test of the round robin matrix. The Figure includes results at 14  $\mu\text{m}$  and 24.5  $\mu\text{m}$  only, since at 1  $\mu\text{m}$  displacement amplitude the friction limit was not reached.

### 5.3. Effects of rig design differences

The two friction rigs have two main design differences, (i) the self-alignment vs rigid alignment of the specimens and (ii) the one-leg contact vs two-leg contact, which probably led to some of the disagreements in both  $\mu$  and  $k_t$  values. These design differences also resulted in advantages and disadvantages in terms of reliability and repeatability of the results. The PoliTO rig showed a larger scatter in the different tests attributed to the higher flexibility in the self-alignment support. In addition, two legs are required with the self-aligning system to avoid tilting of the specimens. The two-leg design might lead to setup and measurement challenges since the contact is prone to uneven load distribution on the two legs if not mounted accurately. Different results can be obtained depending on which leg is measured and which leg is moving more due to a potential rotation of the specimen around its contacting leg. Consequently, great care is required during setup for this type of specimen, and some improvements in the displacement measurements may need to be considered to minimise the sensitivity of the setup with regards to the measurement location. On the positive side, this variability made it possible to gain several insights into the kinematic dependency of the contact stiffness since a large variation in the worn areas could be observed, see e.g. the discussion of Fig. 15.

The Imperial specimens were instead rigidly fixed with slightly curved contact interfaces, and this enabled better repeatability of the experiments, with similar worn areas of contact achieved after each test. However, because of this rigidity, the Imperial rig is limited to relatively small areas of contact. In fact, full worn contact areas could only be reached for the smallest nominal area of contact of 1  $\text{mm}^2$  during the 2.5 h tests, while fully worn areas were easily reached in the PoliTO rig with the help of the self-alignment, even for very large 40  $\text{mm}^2$  areas. A significant increase in testing time in the Imperial rig may have led to fully developed contacts for the larger specimens as well but, due to the large number of tests that had to be conducted, this was not possible. However, all  $k_t$  values were normalised with regards to the actual worn area, which partially eliminated the need of fully worn contact interfaces.

In conclusion, the choice of whether to use a rigid or self-aligning system depends on the purpose of the test. If more repeatable tests and interface conditions are required, a rigid setup is preferable, at the cost of only testing smaller areas of contact, limited topographies and requiring longer testing times. Instead, if more complex and large interfaces are to be tested, a self-aligning system is to be used since it allows for a wider range of test setups, but great care is required since the added flexibility of the setup and loading uncertainty could interfere with the measurements.

## 6. Guidelines for providing accurate input contact parameters for nonlinear dynamic analysis of jointed structures

Based on the insights gained during the round robin test, guidelines are here proposed for the measurement and use of  $\mu$  and  $k_t$  as input for the nonlinear dynamic analysis of jointed structures. In addition, all supporting experimental data has been uploaded open access for use by the research community [60].

### 6.1. Tangential contact stiffness

The following suggestions can be given for the correct measurement and use of tangential contact stiffness values:

- $k_t$  has to be normalised by the **worn area of contact** rather than the nominal area of contact. This can be achieved by running a test until the whole nominal contact area wears in, so that a reliable normalisation can be performed with this a priori known value. Alternatively, the worn area of contact must be determined after each test to establish the normalised stiffness value. Due to the strong effect that wear has on the actual contact area, models also need to take this into account since nominal and real worn areas are very rarely the same [4,76]. Some preliminary studies exist in the literature that implemented the wear evolution in nonlinear dynamic analysis, see e.g. [84,85], where the contact stiffness is updated as wear changes the contact interfaces.
- The presented results have shown that the worn area-normalised tangential contact stiffness,  $K_T$ , **increases with increasing normal load** and it **decreases with increasing displacement amplitude**. These dependencies should be included in a nonlinear dynamic analysis in order to obtain improved results. For the specific combination of tested materials and loading conditions, these dependencies are quantified in Table 4. It is proposed here that the displacement dependency can be included, in a first approximation and under similar loading conditions, by considering  $K_T$  values in fully stuck loops 5 times larger than the  $K_T$  in loops with gross slip. The nonlinear dynamic solver should be able to switch between the two cases depending on the existence of gross slip or not. Since this approach might cause convergence issues, numerical analyses should be performed to test its feasibility.
- The stiffness  $k_t$  depends not only on the extension of the worn area, but also on the **spatial distribution of the worn area over the contact**. A worn area distributed in a certain direction stiffens the contact when it moves mainly in that direction and not in others. As a result, it is important to accurately choose the most representative laser measurement locations during experiments for reliable  $k_t$  estimations.

**Table 4**

$\mu$  and  $K_T$  values plus uncertainty bands to be used in nonlinear dynamic analysis for steel on steel contacts. These values are based on the average between Imperial and PoliTO results and are representative of contact interfaces subjected to the following loading conditions: excitation frequency range 100–175 Hz, room temperature, displacement amplitudes below 50  $\mu\text{m}$ , contact pressures below 250 MPa. The nominal areas of contact were below the 40  $\text{mm}^2$  either in a flat-on-flat arrangement or in a quasi-flat arrangement with relatively large curvatures, above 30 mm, if compared to the average 2 mm contact width.  $p$  [MPa] is the normal load divided by the worn area of contact. Also  $K_T$  [ $\text{N}/\mu\text{m}/\text{mm}^2$ ] is normalised by the worn area of contact.

	Stuck/microslip loops	Loops with gross slip
$K_T$ [ $\text{N}/\mu\text{m}/\text{mm}^2$ ]	$31.5\sqrt{p} \pm 11\sqrt{p}$	$6.3\sqrt{p} \pm 2.2\sqrt{p}$
$\mu$	$0.79 \pm 0.06$	$0.79 \pm 0.06$

- Since the contact behaviour depends on where the interfaces get into contact, it consequently strongly depends on the pressure distribution. To account for this effect in nonlinear dynamic analysis, it is of high importance to accurately model the pressure distribution that is expected in the investigated contact, as done in [4,86]. Depending on the pressure distribution, the  $k_t$  values will change according to the laws in Table 4 and, consequently, also the kinematic and vibration behaviour of the contacting components will change.
- When normalised by the worn area,  $K_T$  shows reasonably similar values in both rigs, with differences of less than 70%. These differences are probably due to the inherent experimental uncertainty and to the fact that the contact surface topography of Imperial and PoliTO specimens is slightly different. To account for the experimental uncertainty in nonlinear dynamic analysis, it is suggested to run at least two more sets of simulations adjusting the  $k_t$  values to be 70% higher and 70% lower than the nominal chosen value.
- In stick regime conditions, a running-in increase in  $k_t$  is observed in PoliTO tests, although a worn area is not visible. It was hypothesised that this increase in  $k_t$ , not due to the worn area of contact, is instead due to a plasticity hardening process occurring at the asperities since the stick loops of PoliTO dissipate energy due to the presence of microslip despite the small displacement amplitudes. This increase with the energy dissipated during microslip can be accounted for by using contact models that include also microslip and not only the stick and gross slip conditions.
- To complete the guidelines on the use of the contact stiffness in simulations, a final comment is given on the normal contact stiffness  $k_n$  although it has not been investigated within this study. At a first approximation, it can be considered to be 1.25 times larger than the  $k_t$ , according to the Mindlin ratio defined by contact mechanics [61]. Future studies will be performed on the investigated friction rigs to also study this parameter, by measuring the relative normal displacements with the Digital Image Correlation technique.

## 6.2. Friction coefficient

The following recommendations can be made for the measurement and use of the friction coefficient in nonlinear dynamic analysis:

- $\mu$  is very low (around 0.1) when the interfaces get into contact for the first time. As vibration starts,  $\mu$  rapidly increases at the beginning of the test. This aspect should be considered for the analysis of newly assembled structures, which will have very low friction coefficient values when their contact establishes for the first time. After few vibration cycles, the friction coefficient will stabilise to an average value of 0.79. This reference value is valid for a stainless steel contact within the loading ranges analysed, namely 100–175 Hz excitation frequency at room temperature, 14–50  $\mu\text{m}$  displacement amplitudes and 17–254 N normal loads

corresponding to 5–125 MPa for the observed worn areas of contact. Given the good consistency of the results, it can most likely also be used outside the confirmed range.

- $\mu$  is mostly unaffected by the loading conditions with a small decrease by 15% with increasing normal loads. Since the reasons for this observed decrease are not clear yet, the use of a constant value is proposed here.
- Measurements on the individual rigs for the same loading conditions are quite repeatable with differences within 4% at Imperial and 8% at PoliTO. The PoliTO rig provides larger values than Imperial for the same loading conditions (on average 15% larger). This mismatch is probably due to inaccuracies in the normal load measurement in the rigs and should be a focus for any future improvements of the rigs. To account for the experimental uncertainty in nonlinear dynamic analysis, it is suggested to run at least two more sets of simulations adjusting the  $\mu$  value to be 15% higher and 15% lower than the nominal chosen value. If the structure is assembled for the first time, a simulation with a very low 0.1  $\mu$  value should be run as well.

## 6.3. Guidelines for the use of the friction rigs and design of experiments

- Scan the contact interfaces before and after the experiments with a microscope. Scans before the experiments provide information on the contact surface topographies, which are needed to predict the pressure distribution at the beginning of the tests. Interface scans at the end of the tests are required to measure the extension of the worn area of contact, which is needed to normalise the contact stiffness during the post-processing. If interface scans cannot be acquired at the end of the test, the test should be run long enough so that the full nominal area wears in, and the  $k_t$  can be normalised by the nominal area.
- The steady state in the measured hysteresis loops is reached (or at least approached) on average after roughly thousands Joules of energy dissipated, which in the presented tests was equivalent to more than 1.5 h of running for excitation frequencies in the range of 100–200 Hz, displacement amplitudes larger than 14  $\mu\text{m}$ , normal loads up to 250 N and nominal areas below 40  $\text{mm}^2$ . Hence it is suggested to run tests for at least 1.5 h if the loading conditions are similar or lead to similar amounts of energy dissipated. Note that this value might depend on the tested material, stainless steel in this case, and hence it is suggested to run at least one long test with a different material to get an estimation of the required amount of dissipated energy for reaching steady state.
- Hysteresis loops should be continuously recorded at the beginning of a high-frequency vibration test since significant changes occur during the initial seconds of the tests. After the first minutes, a lower recording rate can be adopted, since hysteresis loops will be more stable.
- Under low normal loads, e.g. below 17 N, instabilities at the interfaces might occur during high-frequency testing. For example, the Imperial rig experienced a chattering phenomenon due to its particular rigidity. It is hence suggested to identify such issues or avoid at all measurements under such low normal loads if accurate input contact parameters estimations are needed for nonlinear dynamic analysis.
- A wide range of nominal areas was investigated, from 1  $\text{mm}^2$  up to 40  $\text{mm}^2$ , to understand which experimental input values are best suited for nonlinear dynamic analysis. Based on the results shown in this article, the answer depends on the accuracy of the numerical simulations. If the real topography of the interface (i.e. its roughness, waviness and form) is well captured with the employed models, then the pressure distributions could be approximated with the simulations. By knowing the exact pressure distributions, accurate  $k_t$  estimations can be provided by performing, at those pressures, simpler and more repeatable

1 mm<sup>2</sup> experiments with a rigid contact approach. However, if the interface is numerically modelled as a nominally flat surface with potentially a rough mesh, then it will be very unlikely that a realistic pressure distribution can be predicted. In that case, experiments with larger contact areas, ideally of the same size and surface topology as the investigated components, would be required to know beforehand the realistic pressure distribution. For larger areas, a self-aligning experimental setup is recommended.

- The significant effect of the contact surface topography on the pressure distribution suggests that particular care should be taken in ensuring that contact interfaces are manufactured according to specifications. Geometric tolerances should be accurately specified in the technical drawings used to manufacture the components to be tested. An important tolerance parameter is the flatness of the contacting interfaces, which is defined as the distance between two sets of parallel planes where the entire referenced surface must lie, expressed in mm [87]. The smallest flatness value defined in the ISO 2768 standard is 0.02 [88], which corresponds to a 20 μm distance in the planes. This flatness definition would not be acceptable for applications where friction contacts are expected to impact the structural response [76] (in the present study a flatness below 0.005 was chosen to guarantee a uniform pressure distribution at the beginning of the tests). The relatively large 0.02 flatness value defined in the standard tolerance specifications suggests that designers should be aware of possible unwanted bumps and wavinesses in critical contact interfaces expected to be nominally flat during operation.
- Note that only room temperature was considered in this round robin in order to simplify the analysis of the results and reduce the complexity of the observed phenomena. However, industrial components such as those in turbomachinery might experience much higher temperatures (above 700 °C) and new physics could occur under those conditions, which have not been investigated here.

## 7. Conclusions

A round robin test campaign was performed on the high-frequency friction test rigs at Imperial College London and Politecnico di Torino. The aim was to increase confidence in the measurement of contact interface parameters used as input for nonlinear dynamic analysis of jointed structures. More than 100 specimen pairs with comparable nominal contact areas were manufactured from the same batch of raw stainless steel. They were used to measure millions of hysteresis loops under a range of loading conditions at room temperature that covered the full range of both test rigs.

Values of friction coefficient,  $\mu$ , and tangential contact stiffness,  $k_t$ , were extracted and compared. Although the two friction rigs presented fundamental design differences, they provided similar values in the measurements. Measured  $\mu$  agreed well with differences below the 15%, probably coming from some uncertainty in the normal load measurements and specimen assembly procedures.  $k_t$  values showed discrepancies up to 70%. These differences were due to the inherent experimental uncertainty and to the fact that the contact surface topographies of the specimens of the two rigs were slightly different. To account for this experimental uncertainty in nonlinear dynamic analysis, it is suggested to run at least two more sets of simulations adjusting the  $k_t$  values to be 70% higher and 70% lower than the nominal chosen value.

It was also shown that  $k_t$  slowly increases during the test because of an increase in the worn area of contact. It is consequently necessary to normalise it by the worn area of contact, rather than by the nominal area of contact as often practised in the literature. The normalised  $k_t$ , here named  $K_T$ , also depended on the spatial distribution of the worn area and not only its extension. A worn area distributed in a certain direction stiffens the contact when it moves mainly in that

direction and not in the others. Hence, the evolution of the worn areas of contact should be included in simulations since it strongly affects the kinematics of the contacting components. With regards to the loading conditions,  $K_T$  increased significantly with increasing normal loads, in accordance with existing literature. It was also shown that  $K_T$ , evaluated right after the load reversal, is much lower in hysteresis loops with gross slip than in fully stuck hysteresis loops measured at lower displacement amplitudes. This  $K_T$  decrease in loops with gross slip is here attributed to a reduced time for the ageing of the asperity contacts at higher velocities, i.e. a velocity dependency, and should be included in contact models.

With regards to the friction coefficient, it rapidly increased at the beginning of the test during the first hysteresis cycles but it did not show a clear dependency on the worn area of contact or on the other loading conditions, except for a slight decrease for increasing normal loads.

Based on those findings, specific guidelines have been proposed to measure more accurately these contact parameters. Experimental insights presented here lay the basis for an improved understanding of contact, friction and wear, and provide useful information to develop more reliable contact models to be used in the nonlinear dynamic analysis of jointed structures. In addition to providing all experimental data open access for use by the research community [60], the authors would also encourage other research groups to participate in this comparative study. More work is required to expand the test range of the round robin test and generalise the findings, also to other materials. By adding a further dataset, the statistical significance of the presented data can also be increased. The addition of more friction rigs would show how measurements change with a different setup. For example, further investigations could be performed to quantify the effect of the distribution and size of worn areas of contact and, hence, better understand how different contact surface topographies and pressure distributions affect the measurements. These and more measurements would eventually validate the proposed hypotheses and increase the confidence in the measured contact parameters, on the way towards fully predictive models for the nonlinear dynamic analysis of jointed structures.

## CRedit authorship contribution statement

**Alfredo Fantetti:** Conceptualization, Investigation, Methodology, Writing – original draft. **Daniele Botto:** Conceptualization, Funding acquisition, Resources, Supervision, Writing – review & editing. **Stefano Zucca:** Conceptualization, Funding acquisition, Resources, Supervision, Writing – review & editing. **Christoph Schwingshackl:** Conceptualization, Funding acquisition, Resources, Supervision, Writing – review & editing.

## Declaration of competing interest

The authors declare that they have no known competing financial interests or personal relationships that could have appeared to influence the work reported in this paper.

## Data availability

The authors will publish research data in the journal Data in Brief.

## Acknowledgements

This research has received funding from the European Union's Horizon 2020 research and innovation program under the Marie Skłodowska-Curie grant agreement No 721865, project acronym "EXPERTISE".

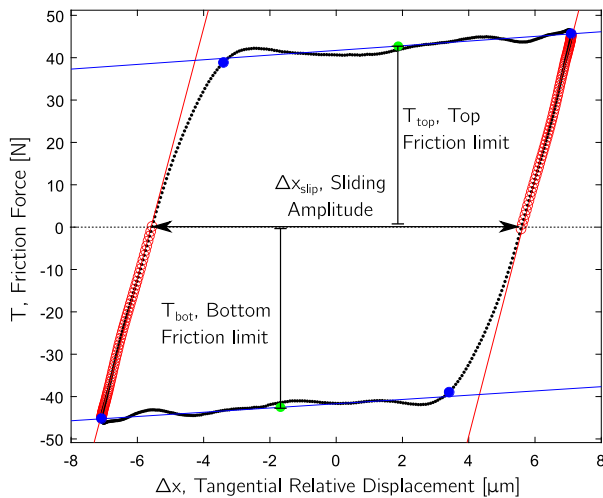


Fig. A.19. Fitting lines used for the extraction of the contact parameters. Two red lines fit the stick part of the loop and two blue lines fit the friction limits.

## Appendix A. Sensitivity study for the accuracy of the contact parameters extraction method

A MATLAB® code has been written to automate the extraction of friction coefficient and tangential contact stiffness, for increased robustness and efficiency. The code is available open access in [60]. Since the contact parameter extraction can be a source of uncertainty in addition to the uncertainty coming from the experiments, a sensitivity study has been performed and described in this Appendix. Fig. A.19 shows a typical post-processed hysteresis loop. The code works by fitting four lines to the hysteresis loop, i.e. two red lines that fit the stick part of the loop and two blue lines that fit the friction limits. From those lines, the contact parameters are extracted as follows.

### A.1. Tangential contact stiffness extraction method

The tangential contact stiffness,  $k_t$ , is calculated as the gradient of the stick portion of the loop from the point of motion reversal to the point where the force is equal to zero, which is far enough from the beginning of the microslip region. Fig. A.19 shows, with red circles, the points used for the linear fitting in the stick region of the hysteresis loop. The value of the slope of the fitted red line is the  $k_t$ .

The accuracy of this extraction method was tested on an individual hysteresis loop by changing the number of points used for the fitting. Fig. A.20a–c shows some examples in which points were added or subtracted for the fitting. The corresponding  $k_t$  values are summarised in Fig. A.20d.

The following conclusions are drawn from the Figure:

(1) The  $k_t$  values (for the considered hysteresis loop) were all within 28.27 and 31.80 N/μm, with a maximum relative standard deviation of 0.9%, being much lower than the deviation due to experimental noise. The low relative standard deviation indicates that this extraction technique is robust since it is not much sensitive to the number of points used for the fitting.

(2) The  $k_t$  is more sensitive to changes in the endpoints than changes to the start points. This is expected since the endpoints are closer to the microslip region and therefore tend to reduce more the slope of the fitted line.

(3)  $k_{tR}$  is slightly larger than  $k_{tL}$ . This is probably due to a slight difference in the normal load of the two friction limits, which was discussed in [13]. However, this effect is acceptable since the change is below 2%.

### A.2. Friction coefficient extraction method

The friction coefficient is calculated with two methods, the energy method and the standard method. Both methods are used in this research since some studies in the literature use only the first method and others only the second [36]. In this way, results could be compared to more studies. The methods are described as follows:

(1) Energy loss formula [45],  $\mu = E/(2N\Delta x_{slip})$ , where  $E$  is the energy dissipated within the hysteresis loop (equal to the area inside the loop, i.e. the integral of the friction force over the relative displacement),  $N$  is the normal load and  $\Delta x_{slip}$  is the sliding amplitude evaluated between the two points with zero friction force as shown in Fig. A.19.

(2) Standard friction coefficient with the equation  $\mu = (T_{top} + T_{bot})/2N$ , where  $T_{top}$  and  $T_{bot}$  are the (absolute) average top and bottom friction limits as shown in Fig. A.19.

For the method 1 (energy friction coefficient), the normal load is known and constant, and it is measured during the test; the energy dissipated is estimated by the integral of the friction force versus the relative displacement; therefore, the only term that can be affected by uncertainty in the extraction method is the sliding amplitude, which is estimated from the relative displacement of the two points of the hysteresis loop where the friction force is zero. A sensitivity study was performed to investigate how much this term varies if different points are used slightly above or below the 0 N friction force as shown in Fig. A.21a. Fig. A.21b shows the result of such investigation with the energy  $\mu$  estimated from different sliding amplitudes. Even for the extreme sliding amplitudes (reference positions +20 and –20 of Fig. A.21a), values do not differ much with a relative standard deviation of only 0.34%. It is concluded that this extraction method is robust and not much affected by the sliding amplitude extraction process.

For the method 2 (standard friction coefficient), the uncertainty might only come from the average friction limits  $T_{top}$  and  $T_{bot}$ . The friction limits are estimated by line fitting all the points between the two blue circles at the top in Fig. A.19 for the top friction limit and all the points between the two blue circles at the bottom for the bottom friction limit. The average value is extracted for each line (resulting in  $T_{top}$  and  $T_{bot}$  of Fig. A.19) and is then divided by the normal load to estimate the friction coefficient. For this method, the sensitivity is performed by changing the position of the limit circles used for the line fitting of the friction limits. Fig. A.21c shows the limit reference positions of the limit circles used for the line fitting. The resulting standard  $\mu$  values are shown in Fig. A.21d. Also for this method, the standard deviation is quite low, only 0.27%, thus indicating that this extraction technique is robust as well. More details on the differences between different friction coefficient estimation methods can be found in the following review<sup>3</sup> [36].

In conclusion, the sensitivity study presented in this section showed that the relative standard deviation is below 0.9% for the contact stiffness extraction and below 0.5% for the friction coefficient extraction. Since the variability for both contact parameters is reasonably low, it is concluded that the developed method is reliable and robust.

<sup>3</sup> Note that a feature of the analysed hysteresis loops is the increasing friction force during gross slip, which is not perfectly constant as expected from the Amontons-Coulomb law of friction. This non-constant behaviour has been described in a previous study [65], which attributed it to local wear scar interaction effects during the reciprocating sliding (e.g. interference of local interlocking peaks and troughs on the worn surfaces).

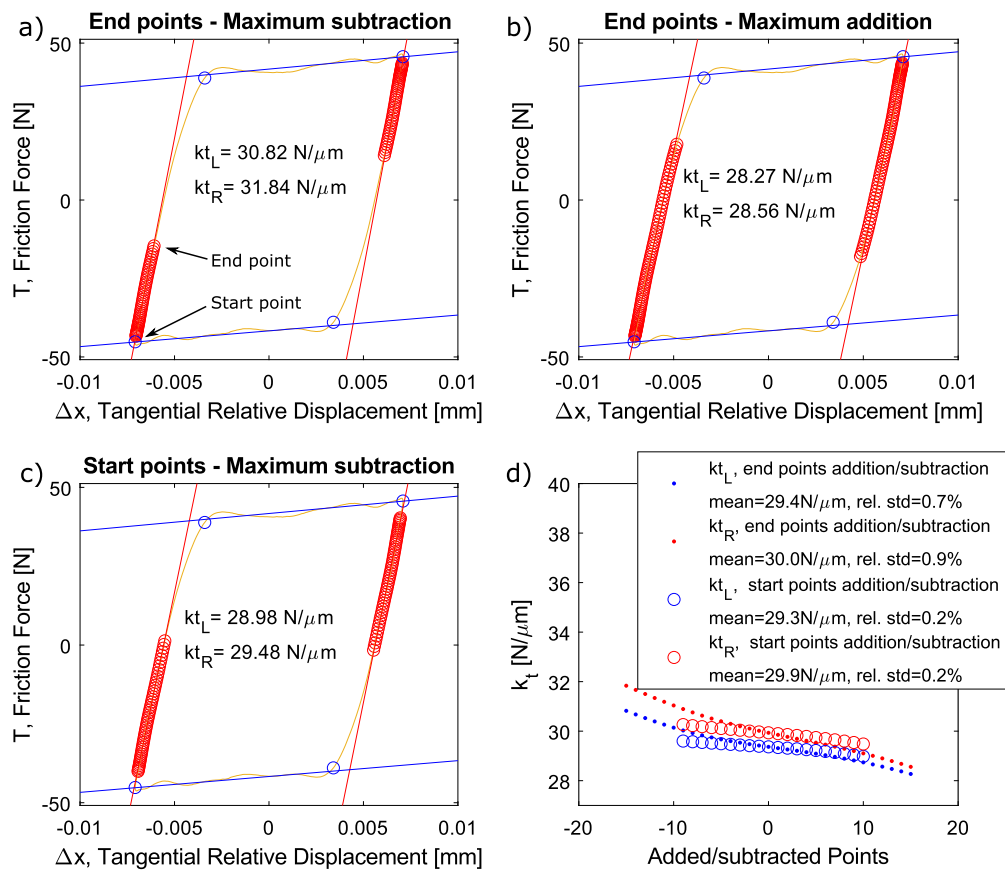


Fig. A.20. Sensitivity study on the tangential contact stiffness: (a–c) hysteresis loops with different number of points chosen for the linear fitting and corresponding  $k_t$  values ( $k_{tL}$  and  $k_{tR}$  are the stiffnesses estimated from the left and right stick regions respectively); (d)  $k_t$  values for different combinations of points used for the fitting.

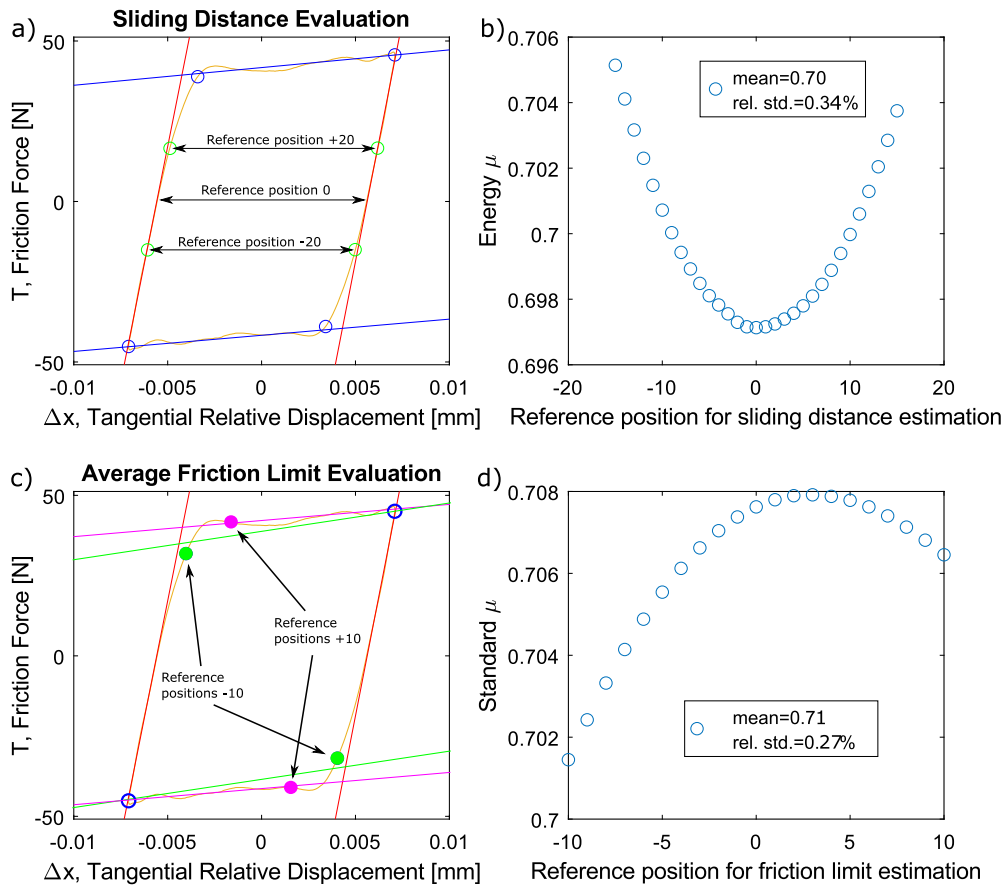


Fig. A.21. Sensitivity study on the friction coefficient (a–b) energy  $\mu$  and (c–d) standard  $\mu$ : (a) Minimum and maximum reference positions for the sliding amplitude estimation for the energy friction coefficient calculation; (b) Energy friction coefficient for sliding amplitudes estimated at different positions; (c) Minimum and maximum reference limit points for the fitting of the friction limits; (d) Standard friction coefficient estimated from friction limits fitted to points limited by different reference positions.

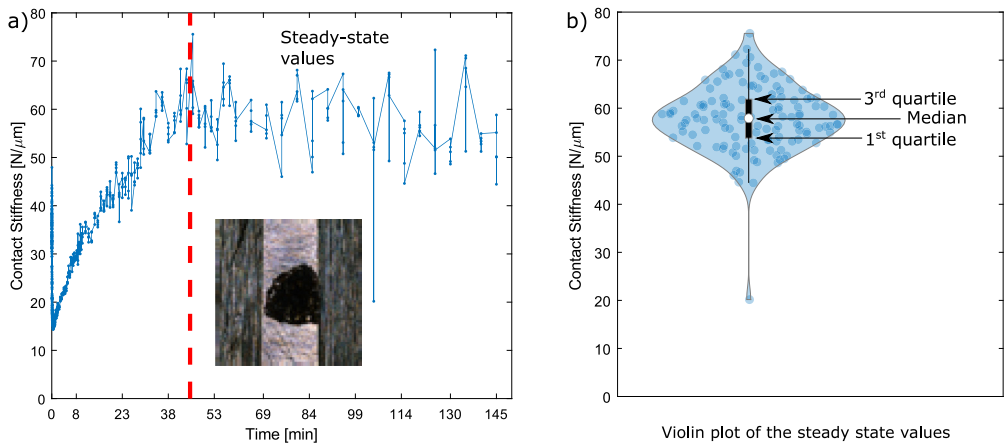
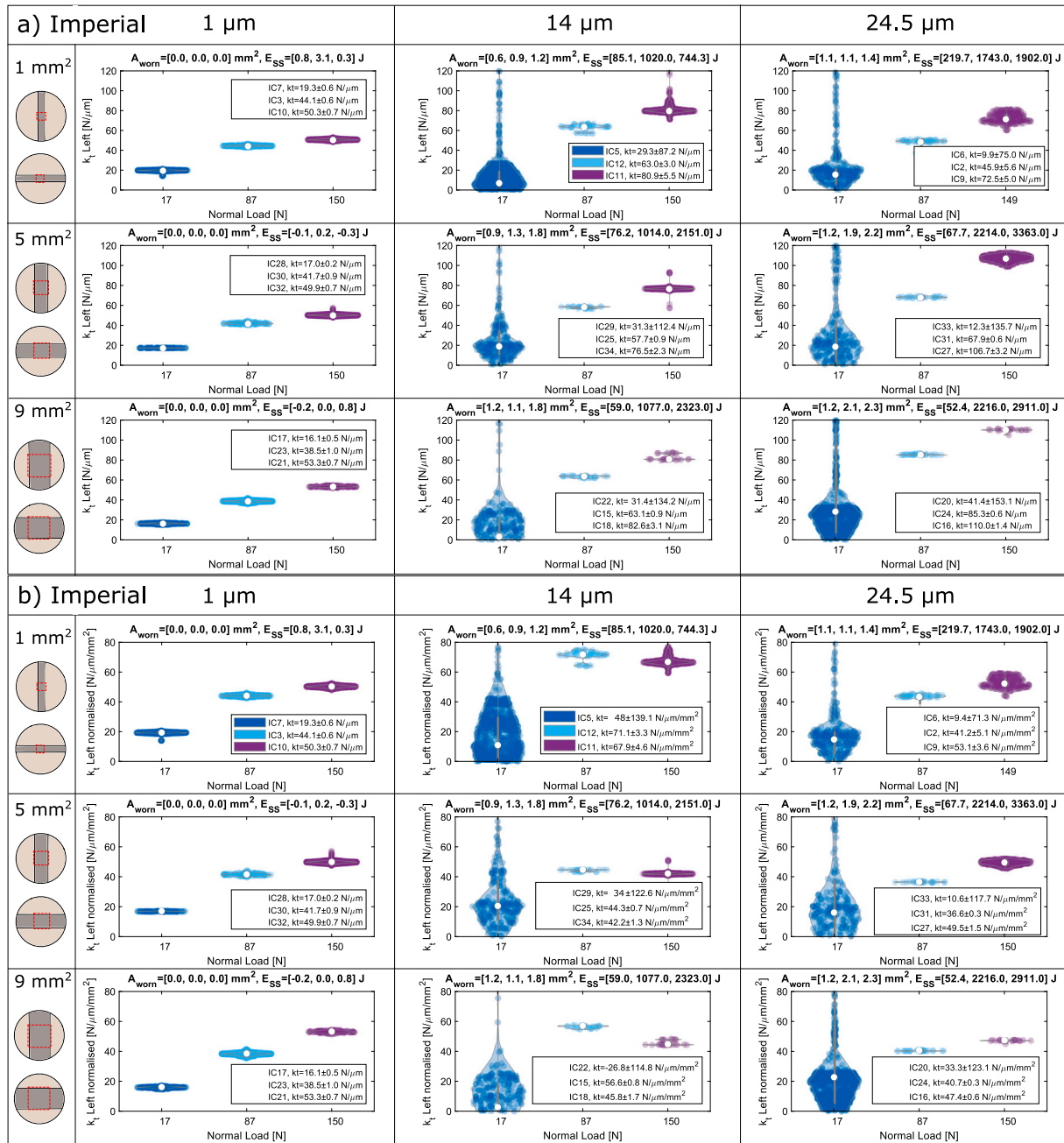


Fig. B.22. (a) Typical evolution of the contact stiffness during a 2.5 h long test, and identification of the steady state values. The specimen interface at the end of the test is also shown; (b) Violin plot of the steady state values of the test in (a). The white marker indicates the median of the data; the black marker indicates the interquartile range (between the 1st and 3rd quartiles); the blue shaded area includes all sample points.

**Appendix B. Analysis of steady state values of contact parameters for each test**

This Appendix shows a detailed analysis of the steady state values of contact parameters for each test. An example of a typical trend is shown in Fig. B.22a. In the case a steady state existed, its beginning was marked manually (as indicated by the vertical red dashed line) and a statistical analysis was performed on the steady state values. Violin

plots [89] were used to plot the statistical distribution of the steady state values since they provide an understanding of the data distribution, while not taking more space than box plots. As an example, Fig. B.22b shows the violin plot of the steady state values of the test in Fig. B.22a. Violin plots of all the tests performed within the round robin are shown in the following Figures to understand the intrinsic uncertainty of the Imperial  $k_t$  (Fig. B.23), PoliTO  $k_t$  (Fig. B.24) and friction coefficients of both rigs (Fig. B.25).



**Fig. B.23.** Violin plots of the steady state values of the (a) tangential contact stiffness,  $k_t$  and (b) worn area normalised tangential contact stiffness,  $k_T$ , of every round robin test on the Imperial friction rig. Each violin corresponds to a different test for one normal load, displacement amplitude and nominal area of contact. The legends indicate the mean and standard deviation of the steady state values of each test. The figure titles indicate the load, the worn areas of the three tests and the energy dissipated when the steady state was reached (note that in most of the tests the steady state was not reached, and the energy represents the energy towards the end of the test). Chattering is often observed during tests at 17 N normal load and that is why the standard deviation is quite large in those tests. Note that tests performed at 1 mm<sup>2</sup> are not normalised by the worn area of contact, because no wear marks were present at the end of the tests.

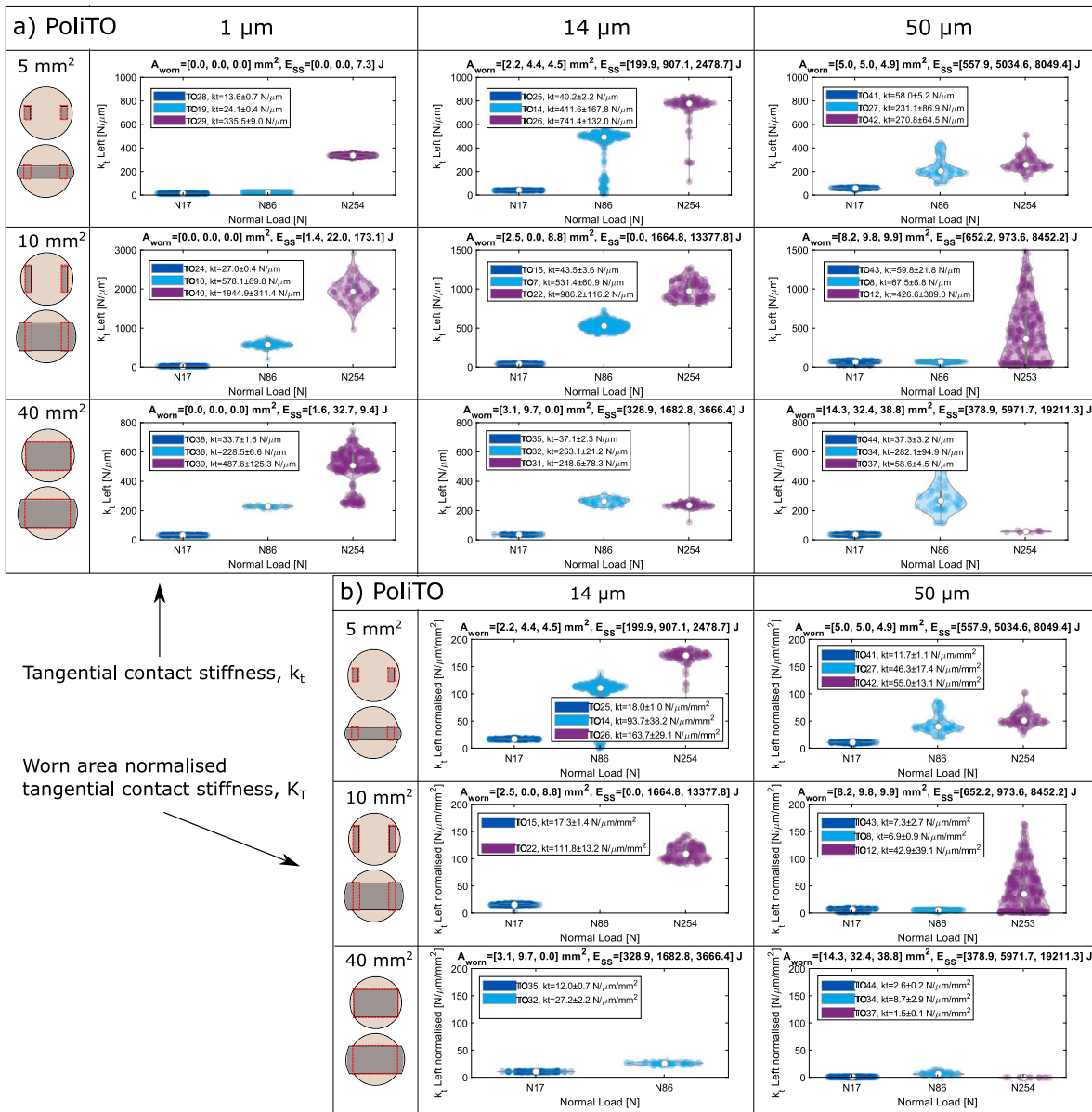
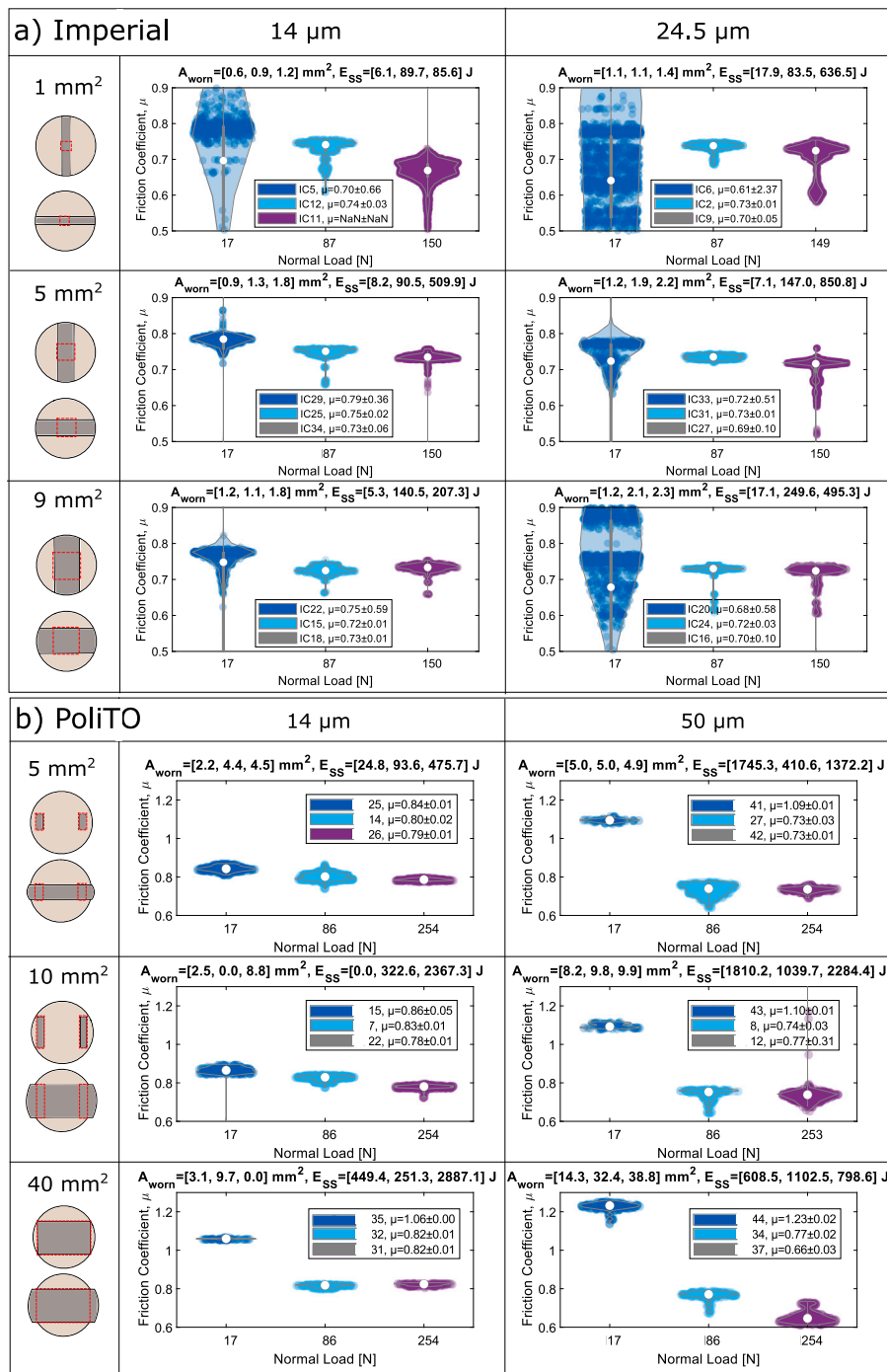


Fig. B.24. Violin plots of the steady state values of the (a) tangential contact stiffness,  $k_t$ , and (b) worn area normalised tangential contact stiffness,  $K_T$ , of every round robin test on the PoliTO friction rig. Each violin corresponds to a different test for one normal load, displacement amplitude and nominal area of contact. The legends indicate the mean and standard deviation of the steady state values of each test. The figure titles indicate the worn areas of the three tests and the energy dissipated when the steady state was reached (note that in some of the tests the steady state was not reached, and the energy represents the energy towards the end of the test). Tests with unmeasured worn areas are not presented.



**Fig. B.25.** Violin plots of the steady state values of the friction coefficient of every round robin test on the (a) Imperial and (b) PoliTO friction rigs. Each violin corresponds to a different test for one normal load, displacement amplitude and nominal area of contact. The legends indicate the mean and standard deviation of the steady state values of each test. The figure titles indicate the worn areas of the three tests and the energy dissipated when the steady state was reached. Chattering was often observed during tests at 17 N normal load at Imperial and that is why the standard deviation is quite large in those tests.

**References**

[1] Brake MR. The mechanics of jointed structures: Recent research and open challenges for developing predictive models for structural dynamics. Springer International Publishing; 2018.

[2] Lavella M, Botto D. Fretting wear of alloy steels at the blade tip of steam turbines. Wear 2019;426–427:735–40. <http://dx.doi.org/10.1016/j.wear.2019.01.039>.

[3] Li D, Botto D, Xu C, Gola M. Fretting wear of bolted joint interfaces. Wear 2020;203411. <http://dx.doi.org/10.1016/j.wear.2020.203411>, URL <https://linkinghub.elsevier.com/retrieve/pii/S004316482030870X>.

[4] Fantetti A, Setchfield R, Schwingshackl C. Nonlinear dynamics of turbine bladed disk with friction dampers: Experiment and simulation. Int J Mech Sci 2023;257. <http://dx.doi.org/10.1016/j.ijmecsci.2023.108510>.

[5] Lavella M, Botto D. Fretting fatigue analysis of additively manufactured blade root made of intermetallic Ti-48Al-2Cr-2Nb alloy at high temperature. Materials 2018;11(7). <http://dx.doi.org/10.3390/ma11071052>.

[6] Yuan J, Fantetti A, Denimal E, Bhatnagar S, Pesaresi L, Schwingshackl C, Salles L. Propagation of friction parameter uncertainties in the nonlinear dynamic response of turbine blades with underplatform dampers. Mech Syst Signal Process 2021;156. <http://dx.doi.org/10.1016/j.ymssp.2021.107673>.

[7] Krack M, Salles L, Thouverez F. Vibration prediction of bladed disks coupled by friction joints. Arch Comput Methods Eng 2017;24(3):589–636. <http://dx.doi.org/10.1007/s0010701701052>.

- [org/10.1007/s11831-016-9183-2](https://doi.org/10.1007/s11831-016-9183-2).
- [8] Ewins DJ. In: Brake MRW, editor. A survey of contact hysteresis measurement techniques. Cham: Springer International Publishing; 2018, p. 161–92. <http://dx.doi.org/10.1007/978-3-319-56818-8>.
- [9] Mulvihill DM, Brunskill H, Kartal ME, Dwyer-Joyce RS, Nowell D. A comparison of contact stiffness measurements obtained by the digital image correlation and ultrasound techniques. *Exp Mech* 2013;53(7):1245–63. <http://dx.doi.org/10.1007/s11340-013-9718-5>.
- [10] Dwyer-Joyce RS. The application of ultrasonic NDT techniques in tribology. 2005. <http://dx.doi.org/10.1243/135065005X9763>.
- [11] Brunskill H, Hunter A, Zhou L, Dwyer Joyce R, Lewis R. An evaluation of ultrasonic arrays for the static and dynamic measurement of wheel-rail contact pressure and area. *Proc Inst Mech Eng J* 2020. <http://dx.doi.org/10.1177/1350650120919889>.
- [12] Starzynski G, Buczkowski R. Ultrasonic measurements of contact stiffness between rough surfaces. *J Tribol* 2014;136. <http://dx.doi.org/10.1115/1.4027132>, URL <http://tribology.asmedigitalcollection.asme.org>.
- [13] Fantetti A, Mariani S, Pesaresi L, Nowell D, Cegla F, Schwingshackl C. Ultrasonic monitoring of friction contacts during shear vibration cycles. *Mech Syst Signal Process* 2021;161:107966. <http://dx.doi.org/10.1016/j.ymssp.2021.107966>, URL <https://linkinghub.elsevier.com/retrieve/pii/S0888327021003617>.
- [14] Pesaresi L, Fantetti A, Cegla F, Salles L, Schwingshackl C. On the use of ultrasound waves to monitor the local dynamics of friction joints. *Exp Mech* 2020;60(1):129–41. <http://dx.doi.org/10.1007/s11340-019-00550-y>, URL <http://link.springer.com/10.1007/s11340-019-00550-y>.
- [15] Wei T, Fantetti A, Cegla F, Schwingshackl C. An optical method to monitor transparent contact interfaces during high frequency shear vibration cycles. *Wear* 2023;204840. <http://dx.doi.org/10.1016/j.wear.2023.204840>, URL <https://linkinghub.elsevier.com/retrieve/pii/S0043164823002235>.
- [16] Sahli R, Pallares G, Ducottet C, Ben Ali IE, Al Akhrass S, Guibert M, Scheibert J. Evolution of real contact area under shear and the value of static friction of soft materials. *Proc Natl Acad Sci USA* 2018;115(3):471–6. <http://dx.doi.org/10.1073/pnas.1706434115>.
- [17] Krick BA, Vail JR, Persson BN, Sawyer WG. Optical in situ micro tribometer for analysis of real contact area for contact mechanics, adhesion, and sliding experiments. *Tribol Lett* 2012;45(1):185–94. <http://dx.doi.org/10.1007/s11249-011-9870-y>.
- [18] Ben-David O, Rubinstein SM, Fineberg J. Slip-stick and the evolution of frictional strength. *Nature* 2010;463(7277):76–9. <http://dx.doi.org/10.1038/nature08676>.
- [19] Ovcharenko A, Halperin G, Etsion I, Varenberg M. A novel test rig for in situ and real time optical measurement of the contact area evolution during pre-sliding of a spherical contact. *Tribol Lett* 2006;23(1):55–63. <http://dx.doi.org/10.1007/s11249-006-9113-9>.
- [20] Zhao G, Xiong Z, Jin X, Hou L, Gao W. Prediction of contact stiffness in bolted interface with natural frequency experiment and FE analysis. *Tribol Int* 2018;127:157–64. <http://dx.doi.org/10.1016/j.triboint.2018.05.044>.
- [21] Soom A, Serpe CI. Normal stiffness and damping at lightly loaded rough planar contacts. *Tribol Int* 2016;100:171–7. <http://dx.doi.org/10.1016/j.triboint.2016.01.007>.
- [22] Cabboi A, Putelat T, Woodhouse J. The frequency response of dynamic friction: Enhanced rate-and-state models. *J Mech Phys Solids* 2016;92:210–36. <http://dx.doi.org/10.1016/j.jmps.2016.03.025>.
- [23] Ahmadian H, Jalali H. Identification of bolted lap joints parameters in assembled structures. *Mech Syst Signal Process* 2007;21(2):1041–50. <http://dx.doi.org/10.1016/j.ymssp.2005.08.015>.
- [24] Nouira D, Tonazzi D, Mezziane A, Baillet L, Massi F. Numerical and experimental analysis of nonlinear vibrational response due to pressure-dependent interface stiffness. *Lubricants* 2020;8(7):73. <http://dx.doi.org/10.3390/lubricants8070073>, URL <https://www.mdpi.com/2075-4442/8/7/73>.
- [25] Wang J, Chen T, Wang XP, Xi Y. Dynamic identification of tangential contact stiffness by using friction damping in moving contact. *Tribol Int* 2019. <http://dx.doi.org/10.1016/j.triboint.2018.10.028>.
- [26] Butlin T, Spelman G, Ghaderi P, Midgley WJ, Umehara R. Predicting response bounds for friction-damped gas turbine blades with uncertain friction coupling. *J Sound Vib* 2019;440:399–411. <http://dx.doi.org/10.1016/j.jsv.2018.08.037>, URL <https://linkinghub.elsevier.com/retrieve/pii/S0022460X18305418>.
- [27] Sherif HA, Kossa SS. Relationship between normal and tangential contact stiffness of nominally flat surfaces. *Wear* 1991;151:49–62.
- [28] Gimpl V, Fantetti A, Klaassen SW, Schwingshackl CW, Rixen DJ. Contact stiffness of jointed interfaces: A comparison of dynamic substructuring techniques with frictional hysteresis measurements. *Mech Syst Signal Process* 2022;171:108896. <http://dx.doi.org/10.1016/j.ymssp.2022.108896>, URL <https://linkinghub.elsevier.com/retrieve/pii/S088832702200084X>.
- [29] Tol S, Özgüven HN. Dynamic characterization of bolted joints using FRF decoupling and optimization. *Mech Syst Signal Process* 2015;54:124–38. <http://dx.doi.org/10.1016/j.ymssp.2014.08.005>.
- [30] Brunetti J, D'Ambrogio W, Fregolat A. Dynamic coupling of substructures with sliding friction interfaces. *Mech Syst Signal Process* 2020;141. <http://dx.doi.org/10.1016/j.ymssp.2020.106731>.
- [31] Saeed Z, Klaassen SW, Fironne CM, Berruti TM, Rixen DJ. Experimental joint identification using system equivalent model mixing in a bladed-disk. *J Vib Acoust* 2020;1–29. <http://dx.doi.org/10.1115/1.4047361>.
- [32] Bowden FP, Tabor D. The friction and lubrication of solids, Vol. 2. OUP; 1964.
- [33] Scholz CH. Earthquakes and friction laws. *Tech. rep.*, 1998, p. 391.
- [34] Li Q, Tullis TE, Goldsby D, Carpick RW. Frictional ageing from interfacial bonding and the origins of rate and state friction. *Nature* 2011;480(7376):233–6. <http://dx.doi.org/10.1038/nature10589>.
- [35] Infante-García D, Marco M, Zabala A, Abbasi F, Giner E, Llavori I. On the role of contact and system stiffness in the measurement of principal variables in fretting wear testing. *Sensors* 2020;20(15):4152. <http://dx.doi.org/10.3390/s20154152>, URL <https://www.mdpi.com/1424-8220/20/15/4152>.
- [36] Llavori I, Zabala A, Aginagalde A, Tato W, Ayerdi JJ, Gómez X. Critical analysis of coefficient of friction derivation methods for fretting under gross slip regime. *Tribol Int* 2020;143. <http://dx.doi.org/10.1016/j.triboint.2019.105988>.
- [37] Toumi S, Fouvry S, Salvia M. Prediction of sliding speed and normal force effects on friction and wear rate evolution in a dry oscillating-fretting PTFE Ti-6Al-4V contact. *Wear* 2017;376–377:1365–78. <http://dx.doi.org/10.1016/j.wear.2017.02.021>.
- [38] Fouvry S, Arnaud P, Mignot A, Neubauer P. Contact size, frequency and cyclic normal force effects on Ti-6Al-4V fretting wear processes: An approach combining friction power and contact oxygenation. *Tribol Int* 2017;113:460–73. <http://dx.doi.org/10.1016/j.triboint.2016.12.049>.
- [39] Done V, Kesavan D, Krishna RM, Chaise T, Nelias D, Lu W, Zhang P, Liu X, Zhai W, Zhou M, Luo J, Zeng W, Jiang X. Semi analytical fretting wear simulation including wear debris. *Tribol Int* 2017;109:1–9. <http://dx.doi.org/10.1016/j.triboint.2016.12.012>, [arXiv:15334406](https://arxiv.org/abs/15334406).
- [40] Lu W, Zhang P, Liu X, Zhai W, Zhou M, Luo J, Zeng W, Jiang X. Influence of surface topography on torsional fretting wear under flat-on-flat contact. *Tribol Int* 2017;109:367–72. <http://dx.doi.org/10.1016/j.triboint.2017.01.001>.
- [41] Eriten M, Polycarpou AA, Bergman LA. Development of a lap joint fretting apparatus. *Exp Mech* 2011;51(8):1405–19. <http://dx.doi.org/10.1007/s11340-010-9458-8>.
- [42] Lampaert V, Al-Bender F, Swevers J. Experimental characterization of dry friction at low velocities on a developed tribometer setup for macroscopic measurements. *Tribol Lett* 2004;16(1):95–105. <http://dx.doi.org/10.1023/B:2903v1>, [arXiv:arXiv:1112.2903v1](https://arxiv.org/abs/1112.2903v1).
- [43] Kubiak KJ, Liskiewicz T, Mathia T. Surface morphology in engineering applications influence of roughness on sliding and wear in dry fretting. *Tribol Int* 2011;44:1427–32.
- [44] Fantetti A, Schwingshackl C. Effect of friction on the structural dynamics of built-up structures: An experimental study. In: Proceedings of the ASME turbo expo 2020: Turbomachinery technical conference and exposition. volume 11: Structures and dynamics: Structural mechanics, vibration, and damping; supercritical CO2. 2020. <http://dx.doi.org/10.1115/GT2020-14945>.
- [45] Lavella M, Botto D, Gola MM. Design of a high-precision, flat-on-flat fretting test apparatus with high temperature capability. *Wear* 2013;302(1–2):1073–81. <http://dx.doi.org/10.1016/j.wear.2013.01.066>.
- [46] Kartal ME, Mulvihill DM, Nowell D, Hills DA. Measurements of pressure and area dependent tangential contact stiffness between rough surfaces using digital image correlation. *Tribol Int* 2011;44(10):1188–98. <http://dx.doi.org/10.1016/j.triboint.2011.05.025>.
- [47] Hoffmann T, Panning L, Wallaschek J. Analysis of contacts in friction damped turbine blades using dimensionless numbers. *J Eng Gas Turbines Power* 2019;141(12). <http://dx.doi.org/10.1115/1.4044481>, URL <https://asmedigitalcollection.asme.org/gasturbinespower/article/doi/10.1115/1.4044481/975419/Analysis-of-Contacts-in-Friction-Damped-Turbine>.
- [48] Umer M, Botto D. Measurement of contact parameters on under-platform dampers coupled with blade dynamics. *Int J Mech Sci* 2019;159:450–8. <http://dx.doi.org/10.1016/j.ijmecsci.2019.06.010>.
- [49] Warmuth AR, Shipway PH, Sun W. Fretting wear mapping: The influence of contact geometry and frequency on debris formation and ejection for a steel-on-steel pair. *Proc R Soc Lond Ser A Math Phys Eng Sci* 2015. <http://dx.doi.org/10.1098/rspa.2014.0291>.
- [50] Baydoun S, Fouvry S. Experimental investigation of adhesive wear area in fretting interface: Application of the contact oxygenation concept. *Tribol Int* 2020;106266. <http://dx.doi.org/10.1016/j.triboint.2020.106266>, URL <https://linkinghub.elsevier.com/retrieve/pii/S0301679X20301080>.
- [51] Hintikka J, Lehtovaara A, Mäntylä A. Fretting-induced friction and wear in large flat-on-flat contact with quenched and tempered steel. *Tribol Int* 2015;92:191–202. <http://dx.doi.org/10.1016/j.triboint.2015.06.008>.
- [52] Hager CH, Sanders JH, Sharma S. Characterization of mixed and gross slip fretting wear regimes in Ti6Al4V interfaces at room temperature. *Wear* 2004;257(1–2):167–80. <http://dx.doi.org/10.1016/j.wear.2003.10.023>.
- [53] Wu J, Yuan R, He Z, Zhang D, Xie Y. Experimental study on dry friction damping characteristics of the steam turbine blade material with nonconforming contacts. *Adv Mater Sci Eng* 2015. <http://dx.doi.org/10.1155/2015/849253>.
- [54] Schwingshackl CW, Petrov EP, Ewins DJ. Measured and estimated friction interface parameters in a nonlinear dynamic analysis. *Mech Syst Signal Process* 2012;28:574–84. <http://dx.doi.org/10.1016/j.ymssp.2011.10.005>.

- [55] de Crevoisier J, Swiergiel N, Champany L, Hild F. Identification of in situ frictional properties of bolted assemblies with digital image correlation, Vol. 52. 2012, p. 561–72. <http://dx.doi.org/10.1007/s11340-011-9518-8>.
- [56] Juoksukangas J, Lehtovaara A, Mäntylä A. Applying the digital image correlation method to fretting contact for slip measurement. *Proc Inst Mech Eng J* 2017;231(4):509–19. <http://dx.doi.org/10.1177/1350650115601695>, SAGE Publications Ltd.
- [57] Chen W, Jin M, Lawal I, Brake MR, Song H. Measurement of slip and separation in jointed structures with non-flat interfaces. *Mech Syst Signal Process* 2019;134:106325. <http://dx.doi.org/10.1016/j.ymssp.2019.106325>, URL <https://linkinghub.elsevier.com/retrieve/pii/S0888327019305461>.
- [58] Brøns M, Kasper TA, Chauda G, Klaassen SW, Schwingshackl CW, Brake MR. Experimental investigation of local dynamics in a bolted lap joint using digital image correlation. *J Vib Acoust* 2020;1–24. <http://dx.doi.org/10.1115/1.4047699>, URL <https://asmedigitalcollection.asme.org/vibrationacoustics/article/doi/10.1115/1.4047699/1084970/Experimental-investigation-of-local-dynamics-in-a>.
- [59] Chen W, Jana D, Singh A, Jin M, Cenedese M, Kosova G, Brake MR, Schwingshackl CW, Nagarajaiah S, Moore KJ, Noël JP. Measurement and identification of the nonlinear dynamics of a jointed structure using full-field data, part I: Measurement of nonlinear dynamics. *Mech Syst Signal Process* 2022;166. <http://dx.doi.org/10.1016/j.ymssp.2021.108401>.
- [60] Fantetti A, Schwingshackl C, Botto D, Zucca S. Experimental dataset from a round robin test on contact parameters for nonlinear dynamic analysis. *Data in Brief* 2023. in preparation.
- [61] Medina S, Nowell D, Dini D. Analytical and numerical models for tangential stiffness of rough elastic contacts. *Tribol Lett* 2013;49(1):103–15. <http://dx.doi.org/10.1007/s11249-012-0049-y>.
- [62] O'Connor JJ, Johnson KL. The role of surface asperities in transmitting tangential forces between metals. *Wear* 1963;6(2):118–39. [http://dx.doi.org/10.1016/0043-1648\(63\)90125-X](http://dx.doi.org/10.1016/0043-1648(63)90125-X).
- [63] Fantetti A, Tamatam L, Volvert M, Lawal I, Liu L, Salles L, Brake MR, Schwingshackl C, Nowell D. The impact of fretting wear on structural dynamics: Experiment and simulation. *Tribol Int* 2019;138:111–24. <http://dx.doi.org/10.1016/j.triboint.2019.05.023>.
- [64] Jin X, Sun W, Shipway PH. Derivation of a wear scar geometry-independent coefficient of friction from fretting loops exhibiting non-Coulomb frictional behaviour. *Tribol Int* 2016;102(102):561–8. <http://dx.doi.org/10.1016/j.triboint.2016.06.012>.
- [65] Mulvihill DM, Kartal ME, Olver AV, Nowell D, Hills DA. Investigation of non-Coulomb friction behaviour in reciprocating sliding. *Wear* 2011;271(5–6):802–16. <http://dx.doi.org/10.1016/j.wear.2011.03.014>.
- [66] Hintikka J, Lehtovaara A, Mäntylä A. Normal displacements in non-Coulomb friction conditions during fretting. *Tribol Int* 2016;94:633–9. <http://dx.doi.org/10.1016/j.triboint.2015.10.029>.
- [67] Botto D, Cuccovillo F, Iannotti V. Experimental investigation of friction damping in blade root joints. *J Eng Gas Turbines Power* 2022;1–26. <http://dx.doi.org/10.1115/1.4056099>.
- [68] Kendall K, Tabor D. An ultrasonic study of the area of contact between stationary and sliding surfaces. *Proc R Soc Lond Ser A Math Phys Eng Sci* 1971;323:321–40. <http://dx.doi.org/10.1098/rspa.1971.0108>.
- [69] Mohd Tobi AL, Sun W, Shipway PH. Evolution of plasticity-based wear damage in gross sliding fretting of a Ti-6Al-4V non-conforming contact. *Tribol Int* 2017;113:474–86. <http://dx.doi.org/10.1016/j.triboint.2017.01.010>.
- [70] Lavella M. Contact properties and wear behaviour of nickel based superalloy rené 80. *Metals* 2016;6(7):159. <http://dx.doi.org/10.3390/met6070159>, URL [www.mdpi.com/journal/metals](http://www.mdpi.com/journal/metals).
- [71] Yue T, Abdel Wahab M. Finite element analysis of fretting wear under variable coefficient of friction and different contact regimes. *Tribol Int* 2017;107:274–82. <http://dx.doi.org/10.1016/j.triboint.2016.11.044>.
- [72] Zhang DK, Ge SR, Qiang YH. Research on the fatigue and fracture behavior due to the fretting wear of steel wire in hoisting rope. *Wear* 2003;255:1233–7. [http://dx.doi.org/10.1016/S0043-1648\(03\)00161-3](http://dx.doi.org/10.1016/S0043-1648(03)00161-3).
- [73] Suh NP, Sin HC. The genesis of friction. *Wear* 1981;69(1):91–114. [http://dx.doi.org/10.1016/0043-1648\(81\)90315-X](http://dx.doi.org/10.1016/0043-1648(81)90315-X), arXiv:27.
- [74] Hurricks PI. The mechanism of fretting - a review. *Wear* 1970;15:389–409.
- [75] Gastaldi C, Gross J, Scheel M, Berruti TM, Krack M. Modeling complex contact conditions and their effect on blade dynamics. *J Eng Gas Turbines Power* 2021;143(1). <http://dx.doi.org/10.1115/1.4049186>.
- [76] Gastaldi C, Berruti T, Gola MM. The effect of surface finish on the proper functioning of underplatform dampers. *J Vib Acoust* 2020;1–30. <http://dx.doi.org/10.1115/1.4046954>.
- [77] Koh K-H, Griffin JH, Filippi S, Akay A. Characterization of turbine blade friction dampers. *J Eng Gas Turbines Power* 2005;127(4):856. <http://dx.doi.org/10.1115/1.1926312>, URL <http://gasturbinespower.asmedigitalcollection.asme.org/article.aspx?articleid=1423184>.
- [78] Rabinowicz E. The nature of the static and kinetic coefficients of friction. *J Appl Phys* 1951;22(11):1373–9. <http://dx.doi.org/10.1063/1.1699869>.
- [79] Baumberger T, Caroli C. Solid friction from stick-slip down to pinning and aging. *Adv Phys* 2006;55(3–4):279–348. <http://dx.doi.org/10.1080/00018730600732186>, arXiv:0506657.
- [80] Bar-Sinai Y, Aldam M, Spatschek R, Brener EA, Bouchbinder E. Spatiotemporal dynamics of frictional systems: The interplay of interfacial friction and bulk elasticity. *Lubricants* 2019;7(10). <http://dx.doi.org/10.3390/lubricants7100091>.
- [81] Dieterich I, James H, Kilgore BD. Direct observation of frictional contacts: New insights for state-dependent properties. *Tech. rep.*, 1994.
- [82] Kennedy FE. Frictional heating and contact temperature. In: *Tribology of ceramics and composites*. 2011, <http://dx.doi.org/10.1002/9781118021668.ch6>.
- [83] Reddyhoff T, Schmidt A, Spikes H. Thermal conductivity and flash temperature. *Tribol Lett* 2019. <http://dx.doi.org/10.1007/s11249-018-1133-8>.
- [84] Armand J, Salles L, Schwingshackl CW, Süß D, Willner K. On the effects of roughness on the nonlinear dynamics of a bolted joint: A multiscale analysis. *Eur J Mech A* 2018;70(February):44–57. <http://dx.doi.org/10.1016/j.euromechsol.2018.01.005>.
- [85] Tamatam LR, Botto D, Zucca S. A novel test rig to study the effect of fretting wear on the forced response dynamics with a friction contact. *Nonlinear Dynam* 2021. <http://dx.doi.org/10.1007/s11071-021-06658-y>, URL <https://link.springer.com/10.1007/s11071-021-06658-y>.
- [86] Tamatam LR, Botto D, Zucca S. A coupled approach to model wear effect on shrouded bladed disk dynamics. *Int J Mech Sci* 2023;107816. <http://dx.doi.org/10.1016/j.ijmecsci.2022.107816>.
- [87] Flatness description [internet]. 2021, Available from: <https://www.gdandtbasics.com/flatness/> [Accessed: 2021-05-26].
- [88] ISO 2768 [internet]. 2021, Available from: <https://www.plianced.com/compliance-wiki/iso-2768-general-geometrical-tolerances-and-technical-drawings/> [Accessed: 2021-05-26].
- [89] Available from: <https://github.com/bastibe/Violinplot-Matlab> [Accessed: 2023-10-14].